

1 **Modeling** impacts of ice-nucleating particles from marine aerosols on mixed-phase
2 **orographic clouds during 2015 ACAPEX field campaign**

3

4 Yun Lin^{1,2}, Jiwen Fan^{1,*}, Pengfei Li^{3,4}, L. Ruby Leung¹, Paul J. DeMott⁵, Lexie Goldberger¹,
5 Jennifer Comstock¹, Ying Liu¹, Jong-Hoon Jeong^{1,2}, Jason Tomlinson¹

6

7 ¹ Atmospheric Sciences and Global Change Division, Pacific Northwest National Laboratory,
8 Richland, WA 99352

9 ² Joint Institute for Regional Earth System Science and Engineering (JIFRESSE), University of
10 California, Los Angeles (UCLA), Los Angeles, CA 90064

11 ³ College of Science and Technology, Hebei Agricultural University, Baoding, Hebei
12 14 071000, P.R. China

13 ⁴ Research Center for Air Pollution and Health; Key Laboratory of Environmental
14 Remediation and Ecological Health, Ministry of Education, College of Environment and
15 Resource Sciences, Zhejiang University, Hangzhou, Zhejiang 310058, P.R. China

16 ⁵ Department of Atmospheric Science, Colorado State University, Fort Collins, CO 80523, USA

17

18 Corresponding author: Jiwen Fan (jiwen.fan@pnnl.gov)

19

20

21

22 **Abstract**

23 A large fraction of annual precipitation over the western United States comes from wintertime
24 orographic clouds associated with atmospheric rivers (ARs). Transported African and Asian dust
25 and marine aerosols from the Pacific Ocean may act as ice-nucleating particles (INPs) to affect
26 cloud and precipitation properties over the region. Here we explored the effects of INPs from
27 marine aerosols on orographic mixed-phase clouds and precipitation at different AR stages for an
28 AR event observed during the 2015 ACAPEX field campaign under low dust ($< 0.02 \text{ cm}^{-3}$)
29 conditions. Simulations were conducted using the chemistry version of the Weather Research
30 and Forecasting model coupled with the spectral-bin microphysics at 1-km grid spacing, with ice
31 nucleation connected with dust and marine aerosols. By comparing against airborne and ground-
32 based observations, accounting for marine INP effects improves the simulation of **AR-**
33 **precipitation**. The marine INPs enhance the formation of ice and snow, leading to less shallow
34 warm clouds but more mixed-phase and deep clouds, **as well as a large spillover effect of**
35 **precipitation after AR landfall**. The responses of cloud and precipitation to marine INPs vary
36 with the AR stages with more significant effects before AR landfall and post-AR than after AR
37 landfall, mainly because the moisture and temperature conditions change with the AR evolution.
38 This work suggests weather and climate models need to consider the impacts of marine INPs
39 since their contribution is notable under low dust conditions despite the much lower relative ice
40 nucleation efficiency of marine INPs.

41

42 **1 Introduction**

43 Atmospheric river (AR) events have great impacts on atmospheric and hydrological
44 processes in the western United States during winter. On a long-term average, AR storms
45 contribute to 20–50% of California’s precipitation totals (Dettinger et al., 2011). Understanding
46 the factors influencing different types of precipitation (rain vs. snow) associated with ARs is
47 crucial for planning and managing regional water resources and hydrologic hazards and
48 improving atmospheric and hydrologic forecasting in the western United States. Rain and snow
49 precipitation produced by orographic clouds over the Sierra Nevada Mountains is closely related
50 to the partitioning between cloud liquid and ice phases, which can be largely modified by aerosol
51 particles (Rosenfeld et al., 2013; Fan et al., 2014, 2017b). However, aerosol-orography-
52 precipitation relationships are complicated, depending on aerosol properties, mountain geometry,
53 cloud phase, temperature, humidity, and flow patterns as reviewed in Chouldhury et al. (2019).

54 Over the western United States, understanding the roles of aerosols, particularly those
55 capable of initiating ice crystal formation in altering clouds and precipitation is still limited,
56 which has motivated recent observational and modeling studies (Ault et al., 2011; Creamean et
57 al., 2013, 2015; Rosenfeld et al., 2013; Fan et al., 2014, 2017b; Martin et al., 2019; Levin et al.,
58 2019). While it has been found that long-range transported aerosols particularly dust particles as
59 ice nucleating particles (INPs) influence clouds and precipitation in the mountainous western
60 United States (Uno et al., 2009; Ault et al., 2011; Creamean et al., 2013), it is also clear from
61 measurements that clouds occurring in and around ARs can also be influenced by INPs with
62 apparent sources from the ocean (Levin et al., 2019).

63 Previous studies showed that INPs can increase total precipitation through the “seeder
64 feeder” mechanism (Choularton and Perry, 1986; Creamean et al., 2013), in which ice crystals

65 that form in the upper portions of orographic clouds can collect droplets and grow to a larger size
66 as they fall through a supercooled liquid layer before reaching the ground. Fan et al. (2014,
67 2017b) found that INPs like dust particles can increase precipitation by enhancing riming and
68 deposition processes in mixed-phase orographic clouds, consistent with other studies (e.g.,
69 Muhlbauer and Lohmann, 2009; Xiao et al., 2015; Hazra et al., 2016; Yang et al., 2020). Fan et
70 al. (2017a) also noted that the relative importance of riming to deposition depends on the mixed-
71 phase cloud temperatures. Despite the importance of INPs in cloud formation and precipitation,
72 they typically have a low abundance and large variations in their nucleating characteristics,
73 especially in terms of the temperatures over which they initiate ice crystal formation (Kanji et al.,
74 2017; Levin et al., 2019). Hence, there is large uncertainty in evaluating INPs impacts on mixed-
75 phase and ice clouds as well as precipitation.

76 Dust and biological particles are known INPs. Biological particles can cause freezing at
77 temperatures as warm as -5°C (Murray et al., 2012). During ARs, the long-range transport of
78 dust or biological particles is highly episodic (Creamean et al., 2013). Sea spray or marine
79 aerosols consisting of sea salt and marine organic carbon resulting from wave breaking and
80 bubble bursting at the ocean surface may also be a source of INPs (Burrows et al., 2013;
81 Vergara-Temprado et al., 2017; McCluskey et al., 2018b; Levin et al., 2019). Recently,
82 McCluskey et al. (2018a) derived an ice nucleation parameterization for INPs from sea spray
83 aerosols based on observations collected at a North Atlantic coastal site and its relation to the
84 marine aerosol surface area. Given the distinct physio-chemical characteristics and the different
85 ice-nucleating efficiency (magnitudes lower than mineral dust; McCluskey et al. 2018a), the
86 impact of marine INPs on cloud and precipitation could be very different from dust or biological
87 particles (DeMott et al., 2016; Kanji et al., 2017). However, studies of marine-sourced INP

88 effects on clouds and associated precipitation are limited (Kanji et al., 2017; Levin et al., 2019).
89 A few previous studies investigated the impacts of marine INPs on precipitation and radiation
90 with global climate models (Hoose et al., 2010; Burrows et al., 2013; Yun and Penner, 2013),
91 albeit without the advantage of direct data on their ice nucleation efficiencies. Further, a detailed,
92 process-level understanding of how marine INPs affect mixed-phase cloud processes and
93 precipitation is lacking.

94 Following the CalWater campaigns in 2009, 2011, 2014, an interagency sponsored study,
95 CalWater 2015, utilized a larger suite of instruments and measurement platforms to study ARs
96 and aerosol-cloud interactions in AR environments (Ralph et al., 2016). As part of CalWater
97 2015, the U.S. Department of Energy sponsored Atmospheric Radiation Measurement (ARM)
98 Cloud Aerosol Precipitation Experiment (ACAPEX) field campaign aimed specifically at
99 improving understanding and modeling of aerosol impacts on winter storms associated with
100 landfalling ARs (Leung et al., 2016). The ACAPEX campaign conducted intensive sampling of
101 clouds and aerosols using instruments on board the ARM Aerial Facility Gulfstream (G-1)
102 aircraft and ARM Mobile Facility on board the research vessel Ron Brown. These measurements
103 were made in conjunction with clouds and aerosols, meteorological, hydrological, and oceanic
104 measurements collected by instruments on three other aircraft and Ron Brown and at a coastal
105 surface station. Collectively, these data provide a unique opportunity to examine the complex
106 interactions among aerosols, orographic clouds, and ARs.

107 A major AR event spanning over 5 - 9 February 2015 occurred during the ACAPEX
108 campaign, producing heavy rainfall with some regions receiving up to 400 mm of total
109 precipitation during the event (Ralph et al., 2016; Cordeira et al., 2017). This AR event was
110 extensively sampled by the G-1 aircraft (Schmid et al., 2014) for characterizing aerosol and

111 cloud properties. During this event, marine aerosols were the main aerosol type and marine INPs
112 were dominant at cloud activation temperatures. Aerosol sampled by G-1 indicated that dust and
113 biological particles were rather scarce in and around ARs, which is in stark contrast to the
114 dominance of dust INPs during the AR events in the CalWater 2011 campaign (Levin et al.,
115 2019). Therefore, the AR event during the ACAPEX campaign provides a rather unique
116 opportunity to explore the role of marine aerosols in the orographic clouds and precipitation
117 associated with landfalling ARs in the western United States.

118 In our previous modeling studies (Fan et al., 2014, 2017b), we implemented an
119 immersion freezing parameterization for dust particles (DeMott et al. 2015) in a spectral-bin
120 microphysics (SBM) scheme to examine the long-range dust effects on AR-associated
121 orographic mixed-phase clouds and precipitation during CalWater 2011. With marine INPs
122 dominating in CalWater 2015/ACAPEX, in this study we implemented the recently developed
123 ice immersion nucleation parameterization for sea spray aerosols by McCluskey et al. (2018b) in
124 the SBM scheme. To explicitly simulate various aerosol types, different from Fan et al. (2014,
125 2017a) who prescribed aerosols based on observations, a chemistry version of the Weather
126 Research and Forecasting model (WRF-Chem) coupled with the SBM (Gao et al., 2016) was
127 employed to predict aerosol properties and their interactions with clouds and radiation for the AR
128 event on 6 - 9 February 2015. We focused on exploring the effects of INPs from sea spray
129 aerosols, in competition with mineral dust INPs, on the orographic mixed-phase clouds and
130 precipitation at different stages of the AR event as thermodynamic conditions evolved with the
131 different AR stages.

132 **2 Model configuration and experiment design**

133 The WRF-Chem version 3.6 coupled with SBM as described in Gao et al. (2016) is
134 employed for model simulations of this study, in which SBM is coupled with the Model for
135 Simulating Aerosol Interactions and Chemistry (MOSAIC; Fast et al., 2006; Zaveri et al., 2008).
136 The SBM scheme is a fast version in which ice crystal and snow (aggregates) are represented
137 with a single size distribution (low-density ice) with a separation at 150 μm in radius, and
138 graupel or hail is for high-density ice represented with an additional size distribution (Khain et
139 al., 2009, 2010; Fan et al., 2012, 2017a). Here we choose the graupel version since hail is not one
140 of the major cloud hydrometeors in the case we simulate. The fall speed power law relationships
141 for ice/snow and graupel are depicted in Xue et al. (2017). The WRF-Chem-SBM model is
142 particularly designed to improve simulations of aerosol effects on clouds for complicated aerosol
143 compositions and heterogeneous spatial distribution of aerosols. It has been applied in several
144 studies including warm stratocumulus clouds (Gao et al., 2016), thunderstorms (Fan et al. 2020;
145 Zhang et al., 2020), and supercell storms (Lin et al., 2020). Here WRF-Chem-SBM is employed,
146 different from our previous studies in Fan et al. (2014, 2017a) which used WRF-SBM with
147 prescribed aerosols, in order to explicitly simulate various aerosol types including marine
148 aerosols and dust particles.

149 The four-sector MOSAIC aerosol module is chosen for the simulations of aerosols and
150 the CBMZ (Carbon Bond Mechanism version Z) is used for gas-phase chemistry. The MOSAIC
151 module treats nine major aerosol species (sulfate, nitrate, chloride, ammonium, sodium, black
152 carbon, primary organics, other inorganics (OIN), and water). OIN is used as a surrogate of dust
153 and the production of dust is parameterized with the dust transport model DUSTRAN (Shaw et
154 al., 2008). Sea salt aerosol (a combination of sodium and chloride), as a surrogate for all SSA, is

155 parameterized as a function of sea-surface wind speed (Gong et al., 1997b, a). The dry diameters
156 of the particles over the four bins have a range of 0.039–0.156, 0.156–0.624, 0.624–2.5, and 2.5–
157 10.0 μm , respectively. For the total aerosol, aerosol size distribution over each section is
158 represented with a 2-moment approach that predicts aerosol mass and number following a log-
159 normal distribution (Simmel and Wurzler, 2006). For each composition such as dust and sea salt,
160 only the mass mixing ratio in each section is predicted and outputted. The aerosol number
161 mixing ratio in each bin is only predicted for the total aerosol. Therefore, in this study, the dust
162 and sea salt number mixing ratios used for ice nucleation parameterizations were derived based
163 on their respective mass mixing ratios by assuming the same size and density of all particles over
164 each bin, that is,

$$165 \quad N_{i,j} = \frac{m_j}{6\pi(D_j)^3 \rho_i}$$

166 where i denotes the aerosol composition (sea salt or dust here), j denotes the j^{th} aerosol bin, m_j is
167 the total mass mixing ratio of the j^{th} bin, ρ_i is the assumed density (i.e., 2.6 g cm^{-3} for dust and
168 2.2 g cm^{-3} for sea salt), and D_j is the geometric mean diameter of j^{th} bin. The approach for
169 deriving the number mixing ratio for each aerosol component has been used in the literature (i.e.,
170 Zhao et al., 2013). We understand that the assumption that all particles have the same size over
171 each bin may introduce some uncertainty. However, the size distribution of each aerosol
172 component is unknown in the model and any assumption on the size distribution might introduce
173 uncertainty.

174 **2.1 Implementing immersion freezing parameterization for marine INPs**

176 In the original SBM model, the ice nucleation accounting for both deposition ice
177 nucleation and condensation-freezing is parameterized based on Meyers et al. (1992) and Bigg

178 (1953) is employed for immersion and homogeneous drop freezing. Neither of the ice nucleation
 179 parameterizations is connected with aerosols. Bigg (1953) was formulated based on the
 180 stochastic hypothesis where the freezing probability is assumed proportional to drop mass and
 181 the freezing rate is as a function of temperature without involving INPs. Fan et al. (2014, 2017a)
 182 implemented DeMott et al. (2015) as an immersion freezing parameterization to investigate the
 183 effects of dust INPs on orographic mixed-phase clouds and precipitation during CalWater 2011.
 184 We adapted this implementation to WRF-Chem-SBM for this study to connect ice nucleation
 185 with dust particles. Developed based on both laboratory data and field measurements, DeMott et
 186 al. (2015) is an empirical parameterization for immersion freezing of natural mineral dust
 187 particles. INP concentrations are quantified as functions of temperature and the total number
 188 concentration of particles larger than 0.5 μm diameter. In our implementation, the dust number
 189 mixing ratio for each aerosol bin is derived from its mass as detailed in the section above. The
 190 total dust number mixing ratio inputted to DeMott et al. (2015) is the integration over 0.5 -10
 191 μm .

192 To connect ice nucleation with sea spray aerosols, we implemented McCluskey et al.
 193 (2018a, thereafter MC2018), which was developed for quantifying ice nucleating activity by
 194 marine organics over the North Atlantic Ocean, in SBM following a similar approach as the
 195 implementation of DeMott et al. (2015). The nucleation site density in MC2018 is described as

$$196 \quad n_s = \exp(-0.545(T - 273.15) + 1.012)$$

197 where n_s is the nucleation site density (m^{-2}) and T is the temperature (K). With n_s determined by
 198 MC2018, the nucleated ice particle concentration is obtained following Niemand et al. (2012) as

$$199 \quad \sum_{j=1}^n N_j = \sum_{j=1}^n N_{\text{tot},j} \{1 - \exp[-S_{\text{ae},j} n_s(T)]\}$$

200 where $S_{ae,j}$ is the surface area of individual sea spray aerosol particles in the j^{th} bin which is
201 calculated from $\pi D_j^2/4$ (D_j is the geometric-mean diameter), $N_{tot,j}$ is the total sea spray aerosol
202 number in each bin which is derived from its mass as detailed in the section above, and N_j is the
203 ice particle number in each bin. Sea salt particles are used as the surrogate of sea spray aerosols
204 given that most marine organic aerosols exist with coating on the surface of sea salt particles in
205 the size range that dominates surface area (e.g., Prather et al., 2013).

206 Bigg et al. (1953) is employed only for homogeneous drop freezing when the temperature
207 is colder than -37°C . As discussed in Fan et al. (2014), the deposition-condensation freezing is
208 turned off because the simulation with deposition-condensation freezing produces a large
209 number of small ice particles, which is not consistent with the observed mixed-phase cloud
210 properties in the study region. Contact freezing is also turned off due to negligible contributions
211 (Fan et al., 2014).

212 **2.2 Experiment design**

213 Simulations are configured with two nested domains using the nesting down approach
214 (i.e., the inner domain is run separately driven by the outer domain), covering most of the
215 western US (Fig. 1). The outer domain consists of 399×399 grid points with a horizontal grid
216 spacing of 3 km and the inner domain consists of 498×390 grid points with a horizontal grid
217 spacing of 1 km. 50 vertical levels with stretched intervals are configured, with a grid spacing of
218 70 m at the lowest levels and ~ 400 m at the model top. The dynamics time step is 15 seconds for
219 the outer domain and 5 seconds for the inner domain.

220 The simulation for the outer domain starts at 00:00 UTC on February 3 and runs for 48
221 hours for chemistry spin-up using the WRF-Chem-SBM model, driven by global WRF-Chem
222 simulation as the initial and boundary conditions of gas-phase species and aerosols and the

223 Modern-Era Retrospective analysis for Research and Applications, Version 2 (MERRA2; spatial
224 resolution of 0.5 by 0.5 degree and temporal resolution of 6-hourly) as the initial and boundary
225 conditions of meteorological fields. Then the outer domain simulation is reinitialized at 00:00 UTC
226 on February 5 using the meteorological data from MERRA2 to avoid the large error growth in
227 meteorology associated with long-time model integration, although the chemistry simulation is a
228 continuation from the spin-up run and runs until 23:00 UTC on February 8. Given that running the
229 WRF-Chem-SBM fully-coupled model is extremely computationally expensive for 1-km grid
230 spacing in the inner domain, we interpolate aerosol-related quantities such as aerosol composition,
231 hygroscopicity, and mass and number concentrations from the outer domain simulations using
232 bilinear interpolation for the inner-domain simulation to reduce computational cost. This means
233 that we conduct the inner-domain simulation separately with chemistry turned off, and aerosol
234 information is updated hourly using data from the outer domain simulations. The inner-domain
235 simulation is run from 00:00 UTC on February 5 to 23:00 UTC on February 8, and the initial and
236 boundary meteorological conditions are from MERRA2. To validate this approach, we compared
237 the simulation with fully coupled WRF-Chem-SBM for the inner domain simulation and found
238 that the two simulations resemble each other in terms of precipitation (Fig. S1). Therefore, it is a
239 valid approach that saves computation time by about 40%.

240 For emissions data, the U. S. Environment Protection Agency (EPA) National Emission
241 Inventory (NEI) with a 4 km by 4 km horizontal resolution based on the year 2011 rates
242 (NEI2011) is commonly used for anthropogenic emissions in the United States. However, using
243 NEI2011 predicts too large anthropogenic aerosol mass compared with observations. Since the
244 emissions of gaseous species and particulate matter decreased significantly from 2011 to 2015 in
245 California (Table S1), the California Air Resources Board emission inventory in 2015

246 (CARB2015) is used for anthropogenic emissions input for California, while NEI2011 is used
247 for other states in the simulation domain. The use of NEI2011 for other states is acceptable since
248 the lower and middle atmosphere in the simulation domain is dominated by southwesterly winds
249 during the simulation period that transport air pollutants from coastal to inland regions. The use
250 of CARB2015 reduces the simulation of aerosol number concentrations mainly below 2 km. The
251 aerosol concentration averaged over 1-2 km altitudes is about 160 cm^{-3} with CARB2015 and 317
252 cm^{-3} with NEI2015, which is 26% lower and 47% higher than aircraft observations (215 cm^{-3}),
253 respectively. Thus, the simulated aerosol concentrations with CARB2015 are in better agreement
254 with observations.

255 The Model of Emissions of Gases and Aerosols from Nature (MEGAN) with a monthly
256 temporal and 1 km horizontal resolution (Guenther et al., 2012) is used for biogenic emissions.
257 The Rapid Radiative Transfer Model for application to GCMs (RRTMG) is used for shortwave
258 and longwave radiation schemes (Iacono et al., 2008), the Noah Land Surface Model for land
259 surface physics (Chen and Dudhia, 2001), and the Mellor-Yamada-Janjic (MYJ) scheme for
260 planetary boundary layer parameterization (Mellor and Yamada, 1982; Janjić and Prediction,
261 2001). Cumulus parameterization is not considered for the simulations over both domains.

262 Three simulations were carried out over the inner domain for this study to investigate the
263 impacts of marine INPs: (1) The reference case is Bigg, using the default immersion freezing
264 parameterization of Bigg et al. (1953) in SBM which is temperature-dependent only; (2)
265 DM15+MC18, in which both DeMott et al. (2015) and MC2018 parameterizations are used for
266 ice nucleation from dust and marine aerosols, respectively; (3) DM15, using the parameterization
267 of DeMott et al. (2015) for dust aerosols (diameter $> 0.5 \mu\text{m}$) with MC2018 turned off. The
268 impacts of marine INPs are derived by comparing the DM15+MC18 and DM15 simulations.

269

270 **3 Case description and measurements**

271 As introduced earlier, our study case is the AR event occurring during 5 - 9 February
272 2015 during the ACAPEX campaign and made landfall on the coast of Northern California,
273 producing heavy rainfall. Marine aerosols were the main aerosol type. Dust and biological
274 particles were rather scarce in and around the AR (Levin et al., 2019).

275 The AR evolution has three distinct stages: before AR landfall (from 06:00 UTC 5 to
276 18:00 UTC 6 February), after AR landfall (from 18:00 UTC 6 to 12:00 UTC 7 February), and
277 post-AR (from 12:00 UTC 7 to 09:00 UTC 8 February). The three stages can be identified from
278 the change of the integrated water vapor (IWV) with time during the event (Fig. 2a). Before AR
279 landfall, IWV in most of California was relatively low (Fig. 2a, left). The IWV in northern
280 California increased as the AR made landfall at about 18:00 UTC on 6 February and brought
281 ample water vapor to California (Fig. 2a, middle). Heavy orographic precipitation along the
282 Sierra Nevada Mountains occurred during this period. At 12:00 UTC 7 February, the AR started
283 to retreat (Fig. 2a, right), and postfrontal cloud cells formed, with relatively small cloud fraction
284 and precipitation.

285 Vertical profiles of the thermodynamic and kinematic environments at the three stages
286 are shown in Figs. 2b-d. The thermodynamic and kinematic environments significantly varied
287 with the AR stages. After AR landfall, water vapor increased significantly in the lower
288 atmosphere (below 5 km), but the middle and upper levels became drier (dashed, Fig. 2b)
289 compared with the stage before AR landfall (solid). The vertical motion also weakened after AR
290 landfall (Fig. 2d), suggesting that the atmosphere became more stable. At the post-AR stage,
291 moisture above 2-km altitude was reduced compared to after AR landfall. Note that the

292 temperature below 8 km was colder by up to 6 °C at the post-AR stage compared to the previous
293 two stages (Fig. 2c). These differences in the meteorological conditions among the different
294 stages are very important to understand the cloud and precipitation properties and their responses
295 to marine INPs.

296 Extensive in-situ and remote-sensing measurements are used to understand aerosol and
297 cloud properties and evaluate model results. The G-1 aircraft sampled the postfrontal clouds on
298 February 7 during 20:20-20:30 UTC.

299 Aerosol instruments on board the G-1 aircraft included (1) a Droplet Measurement
300 Technologies (DMT) ultrahigh sensitivity aerosol spectrometer (UHSAS), measuring dry fine
301 mode aerosol size spectra of 55–800 nm with sizing uncertainty of 2.5% (Uin, 2016); (2) a
302 Passive Cavity Aerosol Spectrometer Probe (PCASP) for coarse mode aerosol spectra (0.1-3
303 μm) with +/-20% uncertainty in size and +/-16% in concentration (Goldberger, 2020), and (3)
304 Aerosol Time of Flight Mass Spectrometry (ATOFMS) measurements provided the mean
305 fractional number contributions of aerosol source classifications (Levin et al., 2019). Cloud
306 instruments include an FCDP (1.5-50 μm) with ~ 3 μm uncertainty in size (Glienke and Mei,
307 2020), and the two-dimensional stereo (2DS) probe with +/-10 μm size uncertainty to provide
308 cloud particle size spectra (Glienke and Mei, 2019). Uncertainty in the number concentration for
309 both probes follows Poisson's counting statistics. The LWC and IWC are derived from the Water
310 Content Monitor (WCM) on board the G-1 aircraft, an instrument that uses the impact of water
311 on several heated wires as the basis for measuring cloud total water content (TWC) and liquid
312 water content (LWC) from which the ice water content (IWC) can be derived (Baumgardner et
313 al., 2011; Matthews et al., 2015). Wind tunnel measurements indicate that ice contributes <1% to
314 the LWC elements response.

315 The Next Generation Radar (NEXRAD) radar reflectivity measurements were processed
316 and used for model evaluation. The original NEXRAD Level 2 data (polar coordinate) were
317 downloaded from AWS-NOAA NEXRAD S3 data service ([https://registry.opendata.aws/noaa-](https://registry.opendata.aws/noaa-nexrad/)
318 [nexrad/](https://registry.opendata.aws/noaa-nexrad/)). We mapped the data to a Cartesian coordinate with 2 km horizontal resolution and
319 approximately 5 min frequency using the Python ARM Radar Toolkit (Py-ART; Helmus and
320 Colis, 2016). The operational NEXRAD radar reflectivity uncertainties are 2 - 3 dB (Gourley et
321 al., 2003) and theoretical demonstrations with differing raindrop shape models yield radar
322 reflectivity biases of 1.2 dB (Gourley et al., 2009). The observed precipitation rates are from the
323 rain gauge measurements, provided by the NOAA Earth System Research Laboratory's Physical
324 Sciences Division (<https://psl.noaa.gov/data/obs/datadisplay>).

325 **4 Results**

326 **4.1 Model evaluation with observations**

327 We evaluate the model simulations of aerosol and cloud properties and surface
328 precipitation. Figure 3a shows a comparison of modeled aerosol properties including aerosol
329 number concentration and chemical composition from the simulation of DM15+MC18 intended
330 to represent the observed case, with the G-1 aircraft measurements on 7 February. Aerosol
331 properties in all three simulations are similar, and thus only DM15+MC18 is shown. Overall, the
332 simulated aerosol number concentration over the size range of 0.067 - 3 μm is comparable to the
333 observations over the same size range estimated by combining data from UHSAS and PCASP at
334 below 2-km altitude. The simulation overestimates the total aerosol number concentrations by \sim
335 2-times averaged over the altitudes of 2.2-3.2 km. At 2.8 km, the difference between the
336 simulation (219 cm^{-3}) and observations (55 cm^{-3}) is about 4 times. The mean fractional number
337 contributions of aerosol composition classifications measured from ATOFMS are shown in Fig.

338 3b. For comparison with the model, the mean mass contributions of the corresponding aerosol
339 source classifications are computed since the number concentrations of individual aerosol
340 components are not predicted by WRF-Chem (Fig. 3c). Both the observed fractional number
341 contributions and the simulated mass contributions show that marine aerosols are dominant
342 during the AR event, accounting for more than 60% of the total aerosol number based on
343 ATOFMS measurements and total aerosol mass based on the simulation. Although the simulated
344 dust mass fraction is ~14%, the derived number concentration for sizes larger than 0.5 μm is very
345 low (less than 0.02 cm^{-3} , shown in a later figure). This is because the dust number concentration
346 is dominated by small particles (14.71 cm^{-3} for the sizes smaller than 0.5 μm). The number
347 concentrations of the sea salt aerosols are generally three orders of magnitude higher than those
348 of dust, and these numbers populate smaller bins of the aerosol distribution (97% from the first
349 two aerosol size bins) even though the sea salt mass is predominately at larger sizes (96% from
350 the last two size bins).

351 Figure 4 presents an evaluation of precipitation, showing the accumulated precipitation
352 during the AR event from 06:00 UTC 5 February to 09:00 UTC 8 February 2015 (Fig. 4a-b) and
353 the time-series of mean precipitation rates averaged over the observation stations (Fig. 4c-d). The
354 model generally captures the spatial pattern of the observed accumulated precipitation (Fig. 4a)
355 and reproduces the temporal evolution of precipitation (Fig. 4b). Two major precipitation periods
356 in the observations, including AR-induced orographic precipitation and postfrontal precipitation,
357 are generally captured in the simulations, although the simulated postfrontal precipitation occurs
358 several hours later in the simulations compared to the observations. All three simulations predict
359 a narrower but higher peak precipitation compared with the observed wider peak with lower
360 values (Fig. 4c). However, the overestimation of the peak value by DM15+MC18 is lower than

361 the other two (30% vs. 45% for DM15 and 58% for Bigg; Fig. 4c-d). The accumulated
362 precipitation in the southern mountain range (the southern part of white boxes in Fig. 4a) is
363 generally less than 100 mm in observations and less than 120 mm in DM15+MC18 but more
364 than 140 mm in the other two simulations. The mean precipitation over the white box
365 accumulated over the AR period are 89, 128, 130, and 116 mm for observations, Bigg, DM15,
366 and DM15+MC18, respectively. Again, although all three simulations overestimate the
367 precipitation, DM15+MC18 simulates the lowest value and is closer to observations.
368 DM15+MC18 predicts more precipitation (i.e., 48 mm for the mean accumulated precipitation)
369 than the other two simulations (i.e., 45 mm in Bigg and 42 mm in DM15). The simulated
370 precipitation between Bigg and DM15 is very similar **except for more precipitation in Bigg in the**
371 **northern part of the domain (Fig. 4a-b)**, suggesting that in a low dust environment, the
372 temperature-dependent Bigg (1953) parameterization simulates similar ice formation as DeMott
373 et al. (2015). There is a clear spillover effect caused by marine INPs **(Fig. 4a-b, right). That is,**
374 **with marine INPs considered in DM15+MC18, there is a notable decrease in accumulated**
375 **precipitation (~ 30-50 mm) on the windward side but a large increase (~ 50-70 cm) on the lee**
376 **side (Fig. 4b, right).** This is because more ice/snow formed over the windward side falls slower
377 than rain and more of them are transported to the lee side, which will be discussed more in
378 section 4.2.

379 Cloud phase is crucial to radiation and precipitation for mixed-phase clouds, and the
380 glaciation ratio is usually used to represent the cloud phase states. The glaciation ratio is defined
381 as $IWC/(IWC+LWC)$, where LWC and IWC denote liquid and ice water content, respectively.
382 Values less than 0.1 and larger than 0.9 denote the liquid phase and ice phase, respectively, with
383 values between 0.1 and 0.9 for the mixed-phase (Korolev et al., 2003). The G-1 aircraft sampled

384 the postfrontal clouds on February 7 as shown in Fig. 5a. All three simulations cannot capture the
385 observed size of the precipitation cell (Figs. 5b and S2). In the simulations, precipitation is
386 dominated by a few heavy precipitation clusters instead of the observed wide precipitation area.
387 The simulated cells also do not reach the high altitudes found in the observations. The deviations
388 of the simulation from observations for the postfrontal clouds could be because of various
389 reasons such as (a) the long-time model integration time (the 4th day after model initiation) and
390 (b) the spatial mismatch of simulated and observed clouds since those postfrontal clouds are
391 small. Anyhow, DM15+MC18 simulates the largest size of the precipitation cell, with the
392 highest vertical extent among the three simulations.

393 LWC and IWC along both horizontal and vertical flight segments are displayed in Figs.
394 6a-b. IWC is generally 2-4 times larger than LWC in the postfrontal clouds. To compare with
395 observations, the model data are processed by: (a) selecting the grids at a distance from the
396 simulated cell center similar to the distance of the airplane position from the observed postfrontal
397 cell center, and sampling the data at a similar ambient temperature as observed by the aircraft
398 (around -10 °C along the horizontal segment shown in Fig. 6a); (b) accounting for the location
399 mismatch and increasing the sample size in the simulation to be more representative by
400 extending the sampling area to include 20 grids at the front and back of a selected grid along the
401 flight track, mimicking approximately the distance traveled by the G-1 airplane in five minutes;
402 (c) filtering out the sampled grids with values of (LWC + IWC) below the detection limit of
403 WCM (i.e., 0.02 g m⁻³, Thompson et al., 2016). Both horizontal and vertical flight segments are
404 incorporated for comparison.

405 Figure 6c and d shows comparisons of LWC, IWC, and the glaciation ratio of
406 IWC/(IWC+LWC) between the simulations and aircraft measurements. The LWC is

407 overestimated in all three simulations with DM15+MC18 of the largest overestimation (6 times
408 higher than observations), while IWC is underestimated in Bigg and DM15 (nearly an order of
409 magnitude lower in DM15 than observations) (Fig. 6c). DM15+MC18 predicts much higher
410 IWC than the other two simulations, with an overestimation of IWP by ~ 3 times. The mean
411 glaciation ratios fall in the range of 0.1- 0.9 among the simulations (Fig. 6d), indicating that the
412 observed mixed-phase cloud feature is simulated by the model. DM15+MC18 shows a mean
413 ratio of ~ 0.70 , similar to the observed value of 0.74. This shows that the mixed-phase state is
414 well captured when the marine INP effect is considered. In contrast, in Bigg and DM15 with a
415 glaciation ratio of 0.41 or less, the mixed-phase state is liquid-dominated. The inclusion of the
416 marine INP effect improves the simulation of cloud phase states via enhancing heterogeneous ice
417 formation through immersion freezing. **But the overestimated LWC and IWC at this post-AR**
418 **stage might have implications to marine INP effects. Here it is already indicated that the modeled**
419 post-frontal clouds are very sensitive to marine INPs. A detailed examination of how the marine
420 INPs impact ice nucleation and cloud properties will be discussed in the following section.

421

422 **4.2 Marine INP effects under different AR stages**

423 Impacts of the marine INPs transported from the Pacific Ocean on orographic clouds and
424 precipitation are revealed by comparing the simulation of DM15+MC18 with the simulation of
425 DM15.

426 As described in Section 3 about the AR evolution, before AR landfall (from 06:00 UTC 5
427 to 18:00 UTC 6 February), precipitation occurred in northern California. After AR landfall (from
428 18:00 UTC 6 to 12:00 UTC 7 February), heavy orographic precipitation along the Sierra Nevada
429 Mountains occurred (Fig. 7a). At the post-AR stage (from 12:00 UTC 7 to 09:00 UTC 8

430 February), scattered postfrontal cloud cells formed, with relatively small cloud fractions and
431 precipitation (Fig. 7a). The mean water vapor and temperature profiles are very different
432 between different AR stages, but the two simulations – DM15 (blue) and DM15+MC18 (red) –
433 predict very similar results as seen from the overlapping blue and red lines.

434 From the time series of average precipitation rates (Fig. 7a), the effect of marine INPs
435 varies with the different AR stages, from the large increases of precipitation (over 50% in
436 general) before AR landfall (the red dotted line, second y-axis) to no significant effects (a very
437 small increase) after AR landfall. In the first stage (before AR landfall), the total precipitation
438 increases by 36% on average due to the marine INP effect (Fig. 7a and Table 1). There is only a
439 4% increase in the total precipitation after AR landfall. Note that precipitation is small at some
440 point before AR landfall, so the large increases might not mean that much. The total precipitation
441 at the post-AR stage is negligible and the change in domain-mean precipitation from DM15 and
442 DM15+MC18 is also small. Thus, the marine INP effect only significantly increases the total
443 precipitation over the domain at the stage before AR landfall when a moderate amount of
444 precipitation occurs in northern California (Fig. 8a). After AR landfall, precipitation increases
445 significantly. Although the total precipitation is not changed much by the marine INPs, the
446 marine INPs produce a spillover effect featuring reduced precipitation on the windward slope of
447 the mountains but increase precipitation over the lee side (Fig. 8b and Fig. 9e). This is because
448 with the marine INPs, the larger amount of ice/snow that forms on the windward slope is
449 transported to the lee side (Fig. 9d) and grows to a larger size and precipitates as snow. This
450 spillover effect is accompanied by a large reduction of cloud water and rain over the windward
451 side because of the conversion of liquid to ice (Fig. 9b-c). Since the water vapor transport along
452 the cross-section is very similar between DM15 and DM15+MC18 (Fig. 9a), the spillover effect

453 by marine INPs is mainly the result of different cloud microphysical properties instead of
454 meteorological conditions.

455 Even though the total domain precipitation is not changed much by the marine INPs at
456 the latter two stages, the cloud phase and the near-surface precipitation type (i.e., rain or snow)
457 are notably changed (Table 1). The mean glaciation ratio in the mixed-phase is very low in
458 DM15 (0.14, 0.16, and 0.001 for the 1st, 2nd, and 3rd stages, respectively) and is increased in
459 DM15+MC18 to 0.74, 0.59, and 0.36, respectively. We examine the ratio of snow/(rain+snow)
460 in mass mixing ratio at the lowest model level for the changes of the near-surface precipitation
461 type (Fig. 7b). There is negligible snow precipitation near the surface in DM15 and the ratios of
462 snow precipitation are very small during the entire AR event. The snow precipitation ratios
463 increase in DM15+MC18 and the magnitudes vary significantly with different AR stages. On
464 average, the ratio of snow precipitation increases from 0.002, 0.001, <0.001 in DM15 to 0.08,
465 0.04, and 0.13 in DM15+MC18 before AR landfall, after AR landfall, and post-AR, respectively
466 (Table 1). This shows that marine INPs increase snow precipitation and the effect is particularly
467 significant before AR landfall and post-AR. Correspondingly, rain precipitation is reduced
468 (Table 1). This has an important implication for the regional hydrological resource since more
469 snow accumulation in winter increases freshwater resources in the summer while less rain
470 reduces flood risks.

471 The increased snow and reduced rain at the surface correspond to the increased ice water
472 path (IWP) and decreased liquid water path (LWP; Fig. 7c). The mean LWP in DM15+MC18 is
473 reduced by 66%, 46%, and 26% for the three stages relative to DM15, respectively (Table 1). We
474 showed an increased LWC from DM15 to DM15+MC18 in Fig. 6c in the postfrontal cells. Here
475 the decrease in LWC/LWP averaged over the entire post-AR stage is dominated by the strong

476 decrease over the time before the postfrontal cloud formed. Both LWC and IWC are increased by
477 marine INPs as shown in Fig. 6 (see section 4.3 for more discussion). IWP is greatly enhanced
478 by about 8, 5, and 440 times at the three stages, respectively. Interestingly, the total condensate
479 water path (TWP) is increased by the marine INPs (Fig. 7d). On average there are 45%, 29%,
480 and 35% increases in TWP in DM15+MC18 at the three AR stages relative to DM15,
481 respectively (Table 1). The increases in the total condensate water path and the increased surface
482 precipitation (or no change) suggest that marine INPs enhance the conversion of water from the
483 vapor phase to the condensate phase, which will be further discussed later. This is particularly
484 the case before AR landfall, with water vapor content notably reduced in DM15+MC18
485 compared with DM15 (Fig. S3a).

486 Cloud cover is slightly increased during the first two stages (4-5%) in the simulations
487 considering marine INPs, but the change at the post-AR stage is ~ 20% on average, which is very
488 significant. Because both TWP and cloud cover are increased due to the marine INP effect, the
489 cloud radiative forcing (CRF) at TOA gets stronger by 15%, 13%, and 10% for the three AR
490 stages, respectively. Although the cloud phase, precipitation type, and cloud fraction at the post-
491 AR stage have the largest changes among the three stages by the marine INP effect (Table 1), the
492 CRF does not change drastically probably because of the offset between the increase resulting
493 from the increased cloud fraction and TWP and the decrease from the reduced cloud liquid is the
494 largest.

495 Overall, the marine INP effects on TWP, IWP, and snow precipitation are more
496 significant at the first and third stages (i.e., before AR landfall and post-AR) than the stage after
497 AR landfall, but a notable spillover effect is seen after AR made landfall. Cloud and
498 precipitation quantities are more sensitive to marine INPs before AR landfall than after AR

499 landfall, and the responses of TWP/IWP and snow precipitation are particularly drastic at the
500 post-AR stage (Table 1). *As noted earlier, we should not put much attention on the marine INP*
501 *effects at the post-AR stage since our model seems not be able to capture those small cloud cells*
502 *well.* The reasons leading to the different responses at different AR stages are now examined.

503 **4.3 Explaining different marine INP effects at different AR stages**

504 We first examine the temporal evolution of dust and marine aerosol number
505 concentrations, which are derived based on the predicted mass mixing ratios as described in
506 Section 2 and used as input to the DeMott et al. (2015) and MC2018 parameterizations (Fig. 10a,
507 b), as well as their corresponding immersion freezing (i.e., ice nucleation) rates (Fig. 10c, d). The
508 dust concentrations and the corresponding ice nucleation rates (Fig. 10a, c) are about three orders
509 of magnitude lower than those of the marine aerosols (Fig. 10b, d) during the AR events. Ice
510 nucleation from dust is negligible at temperatures warmer than $-15\text{ }^{\circ}\text{C}$ but the ice nucleation from
511 marine aerosols is notable. This is mainly because of three orders of magnitude higher marine
512 aerosol number concentrations from the surface up to 8 km since ice nucleation efficiencies of
513 marine aerosols are about three orders of magnitude lower than mineral dust at any temperature
514 (MC2018). The deep marine aerosol layer during the AR allows notable ice nucleation at
515 temperatures even higher than $-15\text{ }^{\circ}\text{C}$. Homogenous freezing ($< -37\text{ }^{\circ}\text{C}$; Fig. 10d vs. 10c) occurs
516 less in DM15+MC18 because of a larger consumption of liquid drops and supersaturation in the
517 heterogeneous freezing regime. This is commonly seen in convective clouds (e.g., Zhao et al.
518 2019). The clear-sky marine aerosol number concentrations increase from before AR landfall to
519 post-AR as the AR evolved (Fig. 10b). After the AR made landfall, marine aerosols increase
520 significantly as AR strong winds near the ocean surface produce more of them and also transport
521 more to the Sierra Nevada Mountains (Fig. 10b). Despite the significant increase in marine

522 aerosols after AR landfall, the marine INP effects on clouds and precipitation are small at this
523 stage, because the increase of marine aerosols does not increase ice nucleation rates (Fig. 10d).
524 However, at the post-AR stage, the ice nucleation rates from the marine INPs are up to a few
525 times larger than the earlier two stages (Fig. 10d), explaining why the effects on IWP and snow
526 precipitation at the post-AR stage are largest among the three stages.

527 To further understand how and why cloud and precipitation responses to marine INPs are
528 different at different AR stages, we separate clouds into three cloud regimes: a shallow warm
529 cloud regime with cloud top temperature (CTT) warmer than 0 °C, a mixed-phase cloud regime
530 with CTT between -30 and 0 °C, and a deep cloud regime having CTT colder than -30 °C and
531 cloud base temperatures above 0 °C. Figure 11 shows that the marine INP effect consistently
532 shifts the cloud occurrences from the shallow warm cloud regime to mixed-phase and/or deep
533 cloud regimes among the three AR stages. It is noted that the deep cloud regime is enhanced
534 much more at the first and third stages than the second stage, i.e., 22% before AR landfall and
535 235% at the post-AR stage but only 8% after AR landfall. The post-AR stage also has the largest
536 increase in mixed-phase cloud occurrences.

537 Accordingly, the mean cloud depth for each cloud regime is changed by marine INPs,
538 with a decrease for the shallow warm clouds and an increase for the mixed-phase and deep
539 clouds (Fig. 11b). Before AR landfall, the increase in the deep cloud depth is largest while at the
540 post-AR stage, the increase in the mixed-phase cloud depth is the largest. Consistent with a shift
541 in cloud regimes, the total precipitation produced by shallow warm clouds is reduced by 9%,
542 22%, and 16% while the total precipitation produced by deep clouds is increased by 66%, 4%,
543 and 350%, respectively, at the three AR stages (Fig. 11c). Therefore, the large increase in the
544 surface accumulated precipitation by marine INPs before AR landfall (36%) is mainly because of

545 the increase in deep cloud precipitation. The larger occurrence of deep clouds at this stage is
546 consistent with a larger increase in TWP and reduction in moisture. Although the relative
547 increases in deep cloud occurrences and precipitation by marine INPs are very large at the post-
548 AR stage, their occurrences are so small that their contribution to the total precipitation is
549 negligible. **The effects of marine INPs on the postfrontal clouds might differ from the reality
550 since based on very limited measurement data, the model seems not be able to capture those
551 clouds well. The overestimated supercooled LWC can allow for more riming growth which may
552 lead to a larger sensitivity to marine INPs.**

553 How do marine INPs reduce shallow warm clouds but increase mixed-phase and deep
554 clouds and why is this effect larger at the first and third stages? Marine INPs greatly enhance ice
555 and snow number concentrations and mass mixing ratios through immersion freezing, which
556 converts drops to ice or snow particles (Figs. 12a and 13a). The mean number concentrations
557 and mass mixing ratios of ice particles (ice +snow) in mixed-phase and deep cloud regimes are
558 several orders of magnitude higher in DM15+MC18 than in DM15. As detailed in Fan et al.
559 (2017a) which studied the same type of mixed-phase clouds in the same region, more ice/snow
560 particles forming from the immersion freezing enhance the Wegener–Bergeron–Findeisen
561 (WBF) and riming processes (Table 2), converting supercooled drops to ice or snow and leading
562 to more ice/snow but fewer cloud droplets and raindrops (Figs. 12b, c and 13b, c). The
563 reductions of cloud droplet and raindrop number concentrations and mass mixing ratios from
564 DM15 to DM15+MC18 are larger before AR landfall and during post-AR relative to the stage
565 after AR landfall, corresponding to a larger shift to the mixed-phase and deep clouds. Thus, the
566 larger increases in deposition/WBF and riming rates are seen (Table 2).

567 As discussed earlier, the largest ice nucleation rates from marine aerosols at the post-AR
568 stage explain the largest marine INP effects among the three stages. The factors contributing to
569 the larger ice nucleation rates include the increased abundance of marine aerosols compared to
570 the previous two stages (Fig. 10b). In addition, with the ~ 6 °C colder temperatures below 8-km
571 altitudes during the post-AR stage compared to the other two stages, ice nucleation from marine
572 aerosols becomes more efficient (Fig. 10d). The increase in both LWC and IWC and a large
573 increase in cloud fraction for postfrontal cloud cells by the marine INP effect might also be
574 related to small scale thermodynamic changes through the feedback of microphysical changes
575 over the first two AR stages.

576 As for why increases of deep cloud occurrence and precipitation are less significant after
577 AR landfall compared to before AR landfall, first, the moisture increase after AR landfall occurs
578 in the lower atmosphere while the middle- and upper-level atmosphere are much drier than
579 before AR landfall (Fig. 2d), which favors more warm clouds and rain but is less favorable to ice
580 cloud development as indicated by the smallest ratio of snow precipitation (Fig. 7b). For more
581 warm clouds/rain-dominated situations, the enhancement of ice formation would have less
582 influence. Furthermore, in the drier conditions aloft, more ice formation means less efficient
583 growth, thus the impacts on IWC/IWP and precipitation would be smaller. Cloud dynamics
584 (vertical velocity) is not changed much by the marine INP effect at all three stages, indicating
585 that the feedback from the increased latent heating resulting from enhanced deposition and
586 riming does not play an important role here, likely because this is not a convective environment.

587 **5 Conclusion and discussion**

588 We have explored the effects of INPs from sea spray aerosols transported from the
589 Pacific Ocean on wintertime mixed-phase stratiform cloud properties and precipitation

590 associated with atmospheric river (AR) events. This is done by carrying out simulations at a
591 cloud-resolving scale (1 km) using WRF-Chem coupled with the spectral-bin microphysics
592 (SBM) scheme for an AR event observed during the 2015 Atmospheric Radiation Measurement
593 Cloud Aerosol Precipitation Experiment (ACAPEX). We have implemented ice nucleation
594 parameterization for sea spray aerosols (McCluskey et al. 2018a) into SBM to account for the
595 marine INP effect. By comparing with ground-based observations, we show that considering the
596 marine INP effect in the model improves the simulation of AR-precipitation. Based on the
597 evaluation with limited data from aircraft measurements, it appears the marine INP effect
598 improves the cloud phase states (i.e., increased glaciation ratio) in the post-AR but overestimates
599 condensate mass.

600 Through enhancing ice and snow formation, marine INPs greatly enhance WBF and
601 riming processes, which convert liquid clouds to mixed-phase and ice clouds. There is a notable
602 shift in cloud occurrences with reduced shallow warm clouds (44%, 26%, and 7% for before and
603 after AR landfall and the post-AR stages, respectively) and increased mixed-phase (10%, 7%,
604 and 38%) and/or deep cloud regimes (~ 22%, 8%, and 230%) because of the marine INP effect.
605 As a result, large increases in the ice water path (5 times or more), total condensate water path
606 (29% or more), and the ratio of snow precipitation (40 times or more) are seen. There is an
607 enhanced conversion of water from the vapor phase to the condensate phase so the water vapor is
608 generally reduced with the marine INP effect considered.

609 The significance of the above-described marine INP effects varies with the AR stages,
610 with a larger effect before AR landfall and post-AR than after AR landfall that has the dominant
611 precipitation. Note that the marine INP effects on cloud properties and snow precipitation are
612 still notable even at the stage after AR landfall. Although the total precipitation is not much

613 changed, the drastic increase of snow precipitation and reduced rain precipitation at the surface
614 have an important implication for the regional water resources and flood risks since more snow
615 increases freshwater resources while less rain reduces flash flood risks. In addition, at this stage,
616 the marine INPs produce a notable spillover effect with a precipitation decrease (up to 30%) over
617 the windward slope of the mountains but precipitation (snow) over the lee side is doubled,
618 because more ice/snow formed over the windward side falls slower than rain and is more easily
619 transported to the lee side.

620 Several factors can be responsible for the smaller marine INP effects on cloud properties
621 (particularly reduction of shallow warm clouds and increased mixed-phase and deep clouds) and
622 snow precipitation after AR landfall compared with before AR landfall. First, after AR landfall,
623 the moisture is heavily concentrated at the lower atmosphere while the middle- and upper-level
624 atmosphere is much drier than before AR landfall. Therefore, the environment is more warm
625 cloud and rain dominated, limiting the effects of enhanced ice formation. Furthermore, in drier
626 conditions, more ice formation means less efficient growth, thus the impacts on IWC/IWP and
627 precipitation would be smaller.

628 The post AR stage has the largest response of the cloud regime shift and snow
629 precipitation among the three stages, because of the largest ice nucleation rates from the marine
630 aerosols. The larger ice nucleation rates compared with the other two stages are probably
631 because the abundance of marine aerosols is increased and also with ~ 6 °C colder temperatures
632 below 8-km altitudes than the other two stages, ice nucleation from the deep marine aerosol layer
633 is more efficient. **Since our model may not simulate clouds well at the post AR stage based on
634 very limited measurement data, we emphasize that the large responses to marine INPs simulated
635 at this stage might not reflect the effect in reality.**

636 This study suggests that the inclusion of marine INPs enhances orographic precipitation
637 mainly through more efficient growth (deposition and riming) of a larger number of ice particles
638 than liquid droplets, which is consistent with literature studies (Mühlbauer and Lohmann, 2009;
639 Fan et al., 2014, 2017; Xiao et al., 2015). The spillover effect by the increase of CCN has been
640 presented in several previous studies (e.g., Mühlbauer and Lohmann, 2008, 2009; Saleeby et al.,
641 2011, 2013; Carrio and Cotton, 2014; Letcher and Cotton, 2014). To our knowledge, this study is
642 the first to show the spillover effect associated with the INP effect. The prominent spillover
643 effect by the marine INP is different from Fan et al. (2014, 2017) that did not find such an effect
644 by dust INPs. There are a couple of factors that might be responsible for the difference. First,
645 marine INPs are mainly brought by ARs so the windward side gets INP first while dust INPs are
646 not associated with AR so there is no temporal sequence to have dust between the windward and
647 Lee sides. Second, the AR event is different with a different wind direction and speed, which
648 makes the transport of ice/snow to the lee side easier in this case.

649 The marine INP effect revealed in this study is clearly manifested due to the very low
650 dust INP concentrations for this particular situation and the high abundance of marine aerosols
651 during the AR which allows notable ice nucleation even at temperatures higher than -15 °C. This
652 higher abundance of marine aerosols overcomes the fundamental lower efficiency of marine
653 INPs compared to dust INPs. With high dust INPs, the effects of marine INPs might not be as
654 significant since they compete for supercooled liquid drops. Although this is a single case study,
655 the AR event and its evolution are representative. Thus, the study suggests the importance of
656 accounting for marine aerosols as INPs, in addition to long-range transported mineral dust, to
657 simulate winter clouds and precipitation in the western United States in regional and global
658 climate models. We employ an empirical parameterization for marine INPs developed from the

659 data collected over the northern Atlantic Ocean and use sea salt aerosols as a surrogate of sea
660 spray aerosols, which might produce some uncertainties. Nevertheless, the marine INP
661 parameterization appears representative of this region based on Levin et al. (2019). More
662 observational data **particularly on the extended spatial and temporal coverage are needed in the**
663 **western U.S. for (a) evaluating model simulations more robustly, (b) developing ice nucleation**
664 **parameterizations for potentially variable marine organics and (c) understanding marine organics**
665 **emission and chemical mechanisms and accurately simulating marine organics in the model.** As
666 discussed earlier, the conversion of mass to number concentrations over each aerosol bin might
667 introduce some uncertainty to this study, which calls for model developments of predicting the
668 number concentration of each aerosol component.

669

670 **Data availability.**

671 The observational data can be accessed from the ARM data archive,
672 <https://www.arm.gov/research/campaigns/amf2015apex>. The model simulation data will be
673 available through the NERSC data repository after the paper is accepted.

674

675 **Supplement.**

676 The supplement related to this article is available online at:

677

678 **Author contributions.**

679 JF designed the study and model experiments. YL, JF, and PL performed numerical simulations
680 and analyses. JF and YL wrote the paper and other authors commented on it. LRL, PJD, LG, JF,

681 JT, YL, and JHJ contributed by either processing data including model input and observational
682 data or participating in the discussion of results.

683

684 **Competing interests.**

685 The authors declare that they have no conflict of interest.

686 **Acknowledgments.**

687 This research used resources of the PNNL Institutional Computing (PIC), and National Energy
688 Research Scientific Computing Center (NERSC). NERSC is a U.S. DOE Office of Science User
689 Facility operated under Contract No. DE-AC02-05CH11231. Funding for ACAPEX that
690 provides data collected on the G-1 aircraft was supported by the Atmospheric Radiation
691 Measurement (ARM) user facility, a U.S. Department of Energy (DOE) Office of Science user
692 facility managed by the Office of Biological and Environmental Research. The deployment of
693 the G-1 also involved the assistance of many PNNL/ARM field staff including M. Hubbell and
694 C. Eveland who flew the G-1 during ACAPEX. The authors acknowledge California Air
695 Resources Board for providing the 2015 emission inventory data and Dr. Allen White from
696 NOAA's Physical Sciences Laboratory for providing rainfall gauge data, and thank Alyssa
697 Matthews and Jingyu Wang at PNNL and Yuan Wang at JPL for technical/data discussion.

698

699 **Financial support.**

700 This study was supported by the Office of Science of U.S. Department of Energy Biological and
701 Environmental Research through the Regional and Global Model Analysis program area that
702 supports the Water Cycle and Climate Extremes Modeling (WACCeM) Science Focus Area at
703 PNNL and the DOE Early Career Research Program (project # 70071). PNNL is operated for the

704 U.S. Department of Energy (DOE) by Battelle Memorial Institute under contract DE-AC05-
705 76RL01830.

706 **Reference**

- 707 Ault, A. P., Williams, C. R., White, A. B., Neiman, P. J., Creamean, J. M., Gaston, C. J., Ralph,
 708 F. M., and Prather, K. A.: Detection of Asian dust in California orographic precipitation, *J.*
 709 *Geophys. Res.-Atmo.*, 116, 1–15, <https://doi.org/10.1029/2010JD015351>, 2011.
- 710 Baumgardner, D., Brenguier, J. L., Bucholtz, A., Coe, H., DeMott, P., Garrett, T. J., Gayet, J. F.,
 711 Hermann, M., Heymsfield, A., Korolev, A., Kramer, M., Petzold, A., Strapp, W., Pilewskie,
 712 P., Taylor, J., Twohy, C., Wendisch, M., Bachalo, W., and Chuang, P.: Airborne instruments
 713 to measure atmospheric aerosol particles, clouds and radiation: A cook's tour of mature and
 714 emerging technology, *Atmos. Res.*, 102(1), 10–29, [10.1016/j.atmosres.2011.06.021](https://doi.org/10.1016/j.atmosres.2011.06.021), 2011.
- 715 Bigg, E. K.: The Formation of Atmospheric Ice Crystals by the Freezing of Droplets, *Q. J. Roy.*
 716 *Meteorol. Soc.*, 79, 510–519, <https://doi.org/10.1002/qj.49707934207>, 1953.
- 717 Burrows, S. M., Hoose, C., Pöschl, U., and Lawrence, M. G.: Ice nuclei in marine air: Biogenic
 718 particles or dust?, *Atmos. Chem. Phys.*, 13, 245–267, [https://doi.org/10.5194/acp-13-245-](https://doi.org/10.5194/acp-13-245-2013)
 719 2013, 2013.
- 720 Carrió, G.G., Cotton, W.R., 2014. On the buffering of CCN impacts on wintertime orographic
 721 clouds: an idealized examination, *Atmos. Res.* 137, 136–144.
- 722 Chen, F. and Dudhia, J.: Coupling an Advanced Land Surface–Hydrology Model with the Penn
 723 State–NCAR MM5 Modeling System. Part I: Model Implementation and Sensitivity, *Mon.*
 724 *Weather Rev.*, 129, 569–585, [https://doi.org/https://doi.org/10.1175/1520-](https://doi.org/10.1175/1520-0493(2001)129<0569:Caalsh>2.0.Co;2)
 725 0493(2001)129<0569:Caalsh>2.0.Co;2, 2001.
- 726 Choulaton, T. W. and Perry, S. J.: A model of the orographic enhancement of snowfall by the
 727 seeder-feeder mechanism, *Q. J. Roy. Meteorol. Soc.*, 112, 335–345,
 728 <https://doi.org/https://doi.org/10.1002/qj.49711247204>, 1986.
- 729 Choudhury, G., B. Tyagi, J. Singh, C. Sarangi, S.N. Tripathi. Aerosol-orography-precipitation –
 730 a critical assessment, *Atmos. Environ.*, 214 (116831) (2019), pp. 1-19,
 731 [10.1016/j.atmosenv.2019.116831](https://doi.org/10.1016/j.atmosenv.2019.116831).
- 732 Cordeira, J. M., Ralph, F. M., Martin, A., Gaggini, N., Spackman, J. R., Neiman, P. J., Rutz, J. J.,
 733 and Pierce, R.: Forecasting atmospheric rivers during CalWater 2015, *Bull Am. Meteorol.*
 734 *Soc.*, 98, 449–459, <https://doi.org/10.1175/BAMS-D-15-00245.1>, 2017.
- 735 Creamean, J. M., Suski, K. J., Rosenfeld, D., Cazorla, A., DeMott, P. J., Sullivan, R. C., White,
 736 A. B., Ralph, F. M., Minnis, P., Comstock, J. M., Tomlinson, J. M., and Prather, K. A.: Dust
 737 and Biological Aerosols from the Sahara and Asia Influence Precipitation in the Western
 738 U.S, *Science*, 339, 1572–1578, <https://doi.org/10.1126/science.1227279>, 2013.
- 739 Creamean, J. M., Ault, A. P., White, A. B., Neiman, P. J., Ralph, F. M., Minnis, P., and Prather,
 740 K. A.: Impact of interannual variations in sources of insoluble aerosol species on orographic
 741 precipitation over California’s central Sierra Nevada, *Atmos. Chem. Phys.*, 15, 6535–6548,
 742 <https://doi.org/10.5194/acp-15-6535-2015>, 2015.
- 743 DeMott, P. J., Prenni, A. J., Liu, X., Kreidenweis, S. M., Petters, M. D., Twohy, C. H.,
 744 Richardson, M. S., Eidhammer, T., and Rogers, D. C.: Predicting global atmospheric ice
 745 nuclei distributions and their impacts on climate, *Proc. Nat. Acad. Sci. U.S.A.*, 107, 11217–
 746 11222, <https://doi.org/10.1073/pnas.0910818107>, 2010.
- 747 DeMott, P. J., Prenni, A. J., McMeeking, G. R., Sullivan, R. C., Petters, M. D., Tobo, Y.,
 748 Niemand, M., Möhler, O., Snider, J. R., Wang, Z., and Kreidenweis, S. M.: Integrating
 749 laboratory and field data to quantify the immersion freezing ice nucleation activity of

750 mineral dust particles, *Atmos. Chem. Phys.*, 15, 393–409, [https://doi.org/10.5194/acp-15-](https://doi.org/10.5194/acp-15-393-2015)
751 393-2015, 2015.

752 DeMott, P. J., Hill, T. C. J., McCluskey, C. S., Prather, K. A., Collins, D. B., Sullivan, R. C.,
753 Ruppel, M. J., Mason, R. H., Irish, V. E., Lee, T., Hwang, C. Y., Rhee, T. S., Snider, J. R.,
754 McMeeking, G. R., Dhaniyala, S., Lewis, E. R., Wentzell, J. J. B., Abbatt, J., Lee, C.,
755 Sultana, C. M., Ault, A. P., Axson, J. L., Martinez, M. D., Venero, I., Santos-Figueroa, G.,
756 Stokes, M. D., Deane, G. B., Mayol-Bracero, O. L., Grassian, V. H., Bertram, T. H.,
757 Bertram, A. K., Moffett, B. F., and Franc, G. D.: Sea spray aerosol as a unique source of ice
758 nucleating particles, *Proc. Nat. Acad. Sci. U.S.A.*, 113, 5797–5803,
759 <https://doi.org/10.1073/pnas.1514034112>, 2016.

760 Dettinger, M. D., Ralph, F. M., Das, T., Neiman, P. J., and Cayan, D. R.: Atmospheric Rivers,
761 Floods and the Water Resources of California, *Water-Sup.*, 3(2), 445-478,
762 <https://doi.org/10.3390/w3020445>, 2011.

763 Fan, J., Leung, L. R., Li, Z., Morrison, H., Chen, H., Zhou, Y., Qian, Y., and Wang, Y.: Aerosol
764 impacts on clouds and precipitation in eastern China: Results from bin and bulk
765 microphysics, *J. Geophys. Res.*, 117, <https://doi.org/https://doi.org/10.1029/2011jd016537>,
766 2012.

767 Fan, J., Leung, L. R., DeMott, P. J., Comstock, J. M., Singh, B., Rosenfeld, D., Tomlinson, J.
768 M., White, A., Prather, K. A., Minnis, P., Ayers, J. K., and Min, Q.: Aerosol impacts on
769 California winter clouds and precipitation during CalWater 2011: local pollution versus
770 long-range transported dust, *Atmos. Chem. Phys.*, 14, 81–101, [https://doi.org/10.5194/acp-](https://doi.org/10.5194/acp-14-81-2014)
771 14-81-2014, 2014.

772 Fan, J., Han, B., Varble, A., Morrison, H., North, K., Kollias, P., Chen, B., Dong, X.,
773 Giangrande, S. E., Khain, A., Lin, Y., Mansell, E., Milbrandt, J. A., Stenz, R., Thompson,
774 G., and Wang, Y.: Cloud-resolving model intercomparison of an MC3E squall line case:
775 Part I—Convective updrafts, *J. Geophys. Res.-Atmo.*, 122, 9351–9378,
776 <https://doi.org/10.1002/2017JD026622>, 2017a.

777 Fan, J., Leung, L. R., Rosenfeld, D., and DeMott, P. J.: Effects of cloud condensation nuclei and
778 ice nucleating particles on precipitation processes and supercooled liquid in mixed-phase
779 orographic clouds, *Atmos. Chem. Phys.*, 17, 1017–1035, [https://doi.org/10.5194/acp-17-](https://doi.org/10.5194/acp-17-1017-2017)
780 1017-2017, 2017b.

781 Fast, J. D., Gustafson Jr., W. I., Easter, R. C., Zaveri, R. A., Barnard, J. C., Chapman, E. G.,
782 Grell, G. A., and Peckham, S. E.: Evolution of ozone, particulates, and aerosol direct
783 radiative forcing in the vicinity of Houston using a fully coupled meteorology-chemistry-
784 aerosol model, *J. Geophys. Res.-Atmo.*, 111,
785 <https://doi.org/https://doi.org/10.1029/2005jd006721>, 2006.

786 French, J. R., Friedrich, K., Tessorodorf, S. A., Rauber, R. M., Geerts, B., Rasmussen, R. M.,
787 Xue, L., Kunkel, M. L., and Blestrud, D. R.: Precipitation formation from orographic cloud
788 seeding, *Proc. Nat. Acad. Sci. U.S.A.*, 115, 1168 LP – 1173,
789 <https://doi.org/10.1073/pnas.1716995115>, 2018.

790 Gao, W., Fan, J., Easter, R. C., Yang, Q., Zhao, C., and Ghan, S. J.: Coupling spectral-bin cloud
791 microphysics with the MOSAIC aerosol model in WRF-Chem: Methodology and results for
792 marine stratocumulus clouds, *J. Adv. Model. Earth Syst.*, 8, 1289–1309,
793 <https://doi.org/10.1002/2016MS000676>.Received, 2016.

794 Geerts, B., Miao, Q., Yang, Y., Rasmussen, R., and Breed, D.: An Airborne Profiling Radar
795 Study of the Impact of Glaciogenic Cloud Seeding on Snowfall from Winter Orographic
796 Clouds, *J. Atmos. Sci.*, 67, 3286–3302, <https://doi.org/10.1175/2010JAS3496.1>, 2010.

797 Glienke, S. and Mei, F.: Two-Dimensional Stereo (2D-S) Probe Instrument Handbook. Ed. by
798 Robert Stafford, ARM user facility. DOE/SC-ARM-TR-233. 10.2172/1597436, 2019.

799 Glienke, S. and Mei, F.: Fast Cloud Droplet Probe (FCDP) Instrument Handbook. Ed. by Robert
800 Stafford, ARM user facility. DOE/SC-ARM-TR-238. 10.2172/1597469, 2020.

801 Goldberger, L. A.: Passive Cavity Aerosol Spectrometer Probe Aboard Aircraft (PCASP-AIR)
802 with Signal Processing Package 200 Instrument Handbook. Ed. by Robert Stafford, ARM
803 user facility. DOE/SC-ARM-TR-241, 2020.

804 Gong, S. L., Barrie, L. A., and Blanchet, J. P.: Modeling sea-salt aerosols in the atmosphere 1.
805 Model development, *J. Geophys. Res.-Atmo.*, 102, 3805–3818,
806 <https://doi.org/10.1029/96jd02953>, 1997a.

807 Gong, S. L., Barrie, L. A., Prospero, J. M., Savoie, D. L., Ayers, G. P., Blanchet, J. P., and
808 Spacek, L.: Modeling sea-salt aerosols in the atmosphere 2. Atmospheric concentrations and
809 fluxes, *J. Geophys. Res.-Atmo.*, 102, 3819–3830, <https://doi.org/10.1029/96jd03401>, 1997b.

810 Gourley, J., B. Kaney, and Maddox R.: Evaluating the calibrations of radars: A software
811 approach. Preprints, 31st Int. Conf. on Radar Meteorology, Seattle, WA, Amer. Meteor.
812 Soc., 459–462, 2003.

813 Gourley, J. J., Illingworth, A. J., and Tabary, P: Absolute Calibration of Radar Reflectivity Using
814 Redundancy of the Polarization Observations and Implied Constraints on Drop Shapes, *J.*
815 *Atmos. Ocean Technol.*, 26(4), 689-703, 2009

816 Guenther, A. B., Jiang, X., Heald, C. L., Sakulyanontvittaya, T., Duhl, T., Emmons, L. K., and
817 Wang, X.: The Model of Emissions of Gases and Aerosols from Nature version 2.1
818 (MEGAN2.1): an extended and updated framework for modeling biogenic emissions,
819 *Geosci. Model Dev.*, 5, 1471–1492, [https://doi.org/https://doi.org/10.5194/gmd-5-1471-](https://doi.org/https://doi.org/10.5194/gmd-5-1471-2012)
820 2012, 2012.

821 Hazra, A., Padmakumari, B., Maheskumar, R. S., and Chen, J. P.: The effect of mineral dust and
822 soot aerosols on ice microphysics near the foothills of the Himalayas: A numerical
823 investigation, *Atmos. Res.*, 171, 41–55, <https://doi.org/10.1016/j.atmosres.2015.12.005>,
824 2016.

825 Helmus, J. J. and Collis, S. M.: The Python ARM Radar Toolkit (Py-ART), a library for working
826 with weather radar data in the Python programming language, *J. Open Res. Software*, 4,
827 e25, <https://doi.org/10.5334/jors.119>, 2016

828 Hoose, C., Kristjánsson, J. E., and Burrows, S. M.: How important is biological ice nucleation in
829 clouds on a global scale?, *Environ. Res. Lett.*, 5, 24009, [https://doi.org/10.1088/1748-](https://doi.org/10.1088/1748-9326/5/2/024009)
830 9326/5/2/024009, 2010.

831 Iacono, M. J., Delamere, J. S., Mlawer, E. J., Shephard, M. W., Clough, S. A., and Collins, W.
832 D.: Radiative forcing by long-lived greenhouse gases: Calculations with the AER radiative
833 transfer models, *J. Geophys. Res.-Atmo.*, 113,
834 <https://doi.org/https://doi.org/10.1029/2008jd009944>, 2008.

835 Janjić, Z. I. and Prediction, N. C. for E.: Nonsingular implementation of the Mellor-Yamada
836 level 2.5 scheme in the NCEP Meso model, 2001.

837 Kanji, Z. A., Ladino, L. A., Wex, H., Boose, Y., Burkert-Kohn, M., Cziczo, D. J., and Krämer,
838 M.: Overview of Ice Nucleating Particles, *Meteorol. Monogr.* 58, 1.1-1.33,
839 <https://doi.org/10.1175/amsmonographs-d-16-0006.1>, 2017.

840 Khain, A., Lynn, B., and Dudhia, J.: Aerosol Effects on Intensity of Landfalling Hurricanes as
841 Seen from Simulations with the WRF Model with Spectral Bin Microphysics, *J. Atmos.*
842 *Sci.*, 67, 365–384, <https://doi.org/doi:10.1175/2009JAS3210.1>, 2010.

843 Khain, A. P., Leung, L. R., Lynn, B., and Ghan, S.: Effects of aerosols on the dynamics and
844 microphysics of squall lines simulated by spectral bin and bulk parameterization schemes, *J.*
845 *Geophys. Res.-Atmo.*, 114, <https://doi.org/10.1029/2009jd011902>, 2009.

846 Korolev, A. v, Isaac, G. A., Cober, S. G., Strapp, J. W., and Hallett, J.: Microphysical
847 characterization of mixed-phase clouds, *Q. J. Roy. Meteorol. Soc.*, 129, 39–65,
848 <https://doi.org/https://doi.org/10.1256/qj.01.204>, 2003.

849 Letcher, T., Cotton, W.R., 2014. The effect of pollution aerosol on wintertime orographic
850 precipitation in the Colorado Rockies using a simplified emissions scheme to predict CCN
851 concentrations, *J. Appl. Meteorol. Climatol.* 53 (4), 859–872.

852 Levin, E. J. T., DeMott, P. J., Suski, K. J., Boose, Y., Hill, T. C. J., McCluskey, C. S., Schill, G.
853 P., Rocci, K., Al-Mashat, H., Kristensen, L. J., Cornwell, G., Prather, K., Tomlinson, J.,
854 Mei, F., Hubbe, J., Pekour, M., Sullivan, R., Leung, L. R., and Kreidenweis, S. M.:
855 Characteristics of Ice Nucleating Particles in and Around California Winter Storms, *J.*
856 *Geophys. Res.-Atmo.*, 124, 11530–11551, <https://doi.org/10.1029/2019JD030831>, 2019.

857 Lin, Y., Fan, J., Jeong, J.-H., Zhang, Y., Homeyer, C. R., and Wang, J.: Urbanization-Induced
858 Land and Aerosol Impacts on Storm Propagation and Hail Characteristics, *J. Atmos. Sci.*,
859 78, 925–947, <https://doi.org/10.1175/jas-d-20-0106.1>, 2020.

860 Martin, A. C., Cornwell, G., Beall, C. M., Cannon, F., Reilly, S., Schaap, B., Lucero, D.,
861 Creamean, J., Martin Ralph, F., Mix, H. T., and Prather, K.: Contrasting local and long-
862 range-transported warm ice-nucleating particles during an atmospheric river in coastal
863 California, USA, *Atmos. Chem. Phys.*, 19, 4193–4210, [https://doi.org/10.5194/acp-19-](https://doi.org/10.5194/acp-19-4193-2019)
864 4193-2019, 2019.

865 Matthews, A., F. Mei, and Comstock, J.: Water content monitor (WCM-2000), ARM Airborne
866 Facility (AAF). Atmospheric Radiation Measurement (ARM) Climate Research Facility
867 Data Archive, data set acquired 27 Jan 2015 and accessed 10 Jan 2016, 2015.

868 McCluskey, C. S., Ovadnevaite, J., Rinaldi, M., Atkinson, J., Belosi, F., Ceburnis, D., Marullo,
869 S., Hill, T. C. J., Lohmann, U., Kanji, Z. A., O’Dowd, C., Kreidenweis, S. M., and DeMott,
870 P. J.: Marine and Terrestrial Organic Ice-Nucleating Particles in Pristine Marine to
871 Continentally Influenced Northeast Atlantic Air Masses, *J. Geophys. Res.-Atmo.*, 123,
872 6196–6212, <https://doi.org/10.1029/2017JD028033>, 2018a.

873 McCluskey, C. S., Hill, T. C. J., Humphries, R. S., Rauker, A. M., Moreau, S., Stratton, P. G.,
874 Chambers, S. D., Williams, A. G., McRobert, I., Ward, J., Keywood, M. D., Harnwell, J.,
875 Ponsonby, W., Loh, Z. M., Krummel, P. B., Protat, A., Kreidenweis, S. M., and DeMott, P.
876 J.: Observations of Ice Nucleating Particles Over Southern Ocean Waters, *Geophys. Res.*
877 *Lett.*, 45, 11,989-11,997, <https://doi.org/10.1029/2018GL079981>, 2018b.

878 Mellor, G. L. and Yamada, T.: Development of a turbulence closure model for geophysical fluid
879 problems, *Rev. Geophys.*, 20, 851–875,
880 <https://doi.org/https://doi.org/10.1029/RG020i004p00851>, 1982.

881 Meyers, M. P., DeMott, P. J., and Cotton, W. R.: New Primary Ice-Nucleation Parameterizations
882 in an Explicit Cloud Model, *J. Appl. Meteorol.*, 31, 708–721, [https://doi.org/10.1175/1520-](https://doi.org/10.1175/1520-0450(1992)031<0708:NPINPI>2.0.CO;2)
883 0450(1992)031<0708:NPINPI>2.0.CO;2, 1992.

884 Muhlbauer, A., Lohmann, U.: Sensitivity studies of the role of aerosols in warm- phase
885 orographic precipitation in different dynamical flow regimes. *J. Atmos. Sci.* 65 (8), 2522–
886 2542, 2008.

887 Muhlbauer, A. and Lohmann, U.: Sensitivity studies of aerosol-cloud interactions in mixed-
888 phase orographic precipitation, *J. Atmos. Sci.*, 66, 2517–2538,
889 <https://doi.org/10.1175/2009JAS3001.1>, 2009.

890 Murray, B. J., O’Sullivan, D., Atkinson, J. D., and Webb, M. E.: Ice nucleation by particles
891 immersed in supercooled cloud droplets, *Chem. Soc. Rev.*, 41, 6519–6554,
892 <https://doi.org/10.1039/c2cs35200a>, 2012.

893 Niemand, M., Möhler, O., Vogel, B., Vogel, H., Hoose, C., Connolly, P., Klein, H., Bingemer,
894 H., DeMott, P., Skrotzki, J., and Leisner, T.: A Particle-Surface-Area-Based
895 Parameterization of Immersion Freezing on Desert Dust Particles, *J. Atmos. Sci.*, 69, 3077–
896 3092, <https://doi.org/10.1175/jas-d-11-0249.1>, 2012.

897 Ralph, F. M., Prather, K. A., Cayan, D., Spackman, J. R., DeMott, P., Dettinger, M., Fairall, C.,
898 Leung, R., Rosenfeld, D., Rutledge, S., Waliser, D., White, A. B., Cordeira, J., Martin, A.,
899 Helly, J., and Intrieri, J.: CalWater Field Studies Designed to Quantify the Roles of
900 Atmospheric Rivers and Aerosols in Modulating U.S. West Coast Precipitation in a
901 Changing Climate, *Bull. Am. Meteorol. Soc.*, 97, 1209–1228, [https://doi.org/10.1175/bams-](https://doi.org/10.1175/bams-d-14-00043.1)
902 [d-14-00043.1](https://doi.org/10.1175/bams-d-14-00043.1), 2016.

903 Reynolds, D. W.: A Report on Winter Snowpack-Augmentation, *Bull. Am. Meteorol. Soc.*, 69,
904 1290–1300, [https://doi.org/10.1175/1520-0477\(1988\)069<1290:AROWSA>2.0.CO;2](https://doi.org/10.1175/1520-0477(1988)069<1290:AROWSA>2.0.CO;2), 1988.

905 Rosenfeld, D., Chemke, R., Demott, P., Sullivan, R. C., Rasmussen, R., McDonough, F.,
906 Comstock, J., Schmid, B., Tomlinson, J., Jonsson, H., Suski, K., Cazorla, A., and Prather,
907 K.: The common occurrence of highly supercooled drizzle and rain near the coastal regions
908 of the western United States, *J. Geophys. Res.-Atmo.*, 118, 9819–9833,
909 <https://doi.org/10.1002/jgrd.50529>, 2013.

910 Saleeby, S.M., Cotton, W.R., Fuller, J.D.: The cumulative impact of cloud droplet nucleating
911 aerosols on orographic snowfall in Colorado, *J. Appl. Meteorol. Climatol.* 50 (3), 604–625,
912 2011.

913 Saleeby, S.M., Cotton, W.R., Lowenthal, D., Messina, J.: Aerosol impacts on the microphysical
914 growth processes of orographic snowfall. *J. Appl. Meteorol. Climatol.* 52 (4), 834–852,
915 2013.

916 Schmid, B., Tomlinson, J. M., Hubbe, J. M., Comstock, J. M., Mei, F., Chand, D., Pekour, M. S.,
917 Kluzek, C. D., Andrews, E., Biraud, S. C., and McFarquhar, G. M.: The DOE arm aerial
918 facility, *Bull. Am. Meteorol. Soc.*, 95, 723–742, [https://doi.org/10.1175/BAMS-D-13-](https://doi.org/10.1175/BAMS-D-13-00040.1)
919 [00040.1](https://doi.org/10.1175/BAMS-D-13-00040.1), 2014.

920 Shaw, W. J., Jerry Allwine, K., Fritz, B. G., Rutz, F. C., Rishel, J. P., and Chapman, E. G.: An
921 evaluation of the wind erosion module in DUSTRAN, *Atmos. Environ.*, 42, 1907–1921,
922 <https://doi.org/10.1016/j.atmosenv.2007.11.022>, 2008.

923 Simmel, M. and Wurzler, S.: Condensation and activation in sectional cloud microphysical
924 models, *Atmos. Res.*, 80, 218-236, [10.1016/j.atmosres.2005.08.002](https://doi.org/10.1016/j.atmosres.2005.08.002), 2006.

925 Thompson, D. R., McCubbin, I., Gao, B. C., Green, R. O., Matthews, A. A., Mei, F., Meyer, K.
926 G., Platnick, S., Schmid, B., Tomlinson, J., and Wilcox, E.: Measuring cloud
927 thermodynamic phase with shortwave infrared imaging spectroscopy, *J. Geophys. Res.-*
928 *Atmo.*, 121, 9174–9190, <https://doi.org/10.1002/2016JD024999>, 2016.

929 Uin, J.: Ultra-High-Sensitivity Aerosol Spectrometer (UHSAS) Instrument Handbook. Ed. by
930 Robert Stafford, DOE ARM Climate Research Facility. DOE/SC-ARM-TR-163, 2016.

931 Uno, I., Eguchi, K., Yumimoto, K., Takemura, T., Shimizu, A., Uematsu, M., Liu, Z., Wang, Z.,
932 Hara, Y., and Sugimoto, N.: Asian dust transported one full circuit around the globe, *Nat.*
933 *Geosci.*, 2, 557–560, <https://doi.org/10.1038/ngeo583>, 2009.

934 Vali, G., DeMott, P. J., Möhler, O., and Whale, T. F.: Technical Note: A proposal for ice
935 nucleation terminology, *Atmos. Chem. Phys.*, 15, 10263–10270,
936 <https://doi.org/10.5194/acp-15-10263-2015>, 2015.

937 Vergara-Temprado, J., Murray, B. J., Wilson, T. W., O’Sullivan, D., Browse, J., Pringle, K. J.,
938 Ardon-Dryer, K., Bertram, A. K., Burrows, S. M., Ceburnis, D., Demott, P. J., Mason, R.
939 H., O’Dowd, C. D., Rinaldi, M., and Carslaw, K. S.: Contribution of feldspar and marine
940 organic aerosols to global ice nucleating particle concentrations, *Atmos. Chem. Phys.*, 17,
941 3637–3658, <https://doi.org/10.5194/acp-17-3637-2017>, 2017.

942 Xiao, H., Yin, Y., Jin, L., Chen, Q., and Chen, J.: Simulation of the effects of aerosol on mixed-
943 phase orographic clouds using the WRF model with a detailed bin microphysics scheme,
944 *Atmos. Sci. Lett.*, 120, 8345–8358, <https://doi.org/https://doi.org/10.1002/2014JD022988>,
945 2015.

946 Xue, L., Fan, J., Lebo, Z. et al.: Idealized Simulations of a Squall Line from the MC3E Field
947 Campaign Applying Three Bin Microphysics Schemes: Dynamic and Thermodynamic
948 Structure, *Mon. Wea. Rev.*, 145, 4789- 4812, <https://doi.org/10.1175/MWR-D-16-0385.1>,
949 2017.

950 Yang, Y., Sun, J., Zhu, Y., and Zhang, T.: Examination of the impacts of ice nuclei aerosol
951 particles on microphysics, precipitation and electrification in a 1.5D aerosol-cloud bin
952 model, *J. Aerosol Sci.*, 140, 105440, <https://doi.org/10.1016/j.jaerosci.2019.105440>, 2020.

953 Yun, Y. and Penner, J. E.: An evaluation of the potential radiative forcing and climatic impact of
954 marine organic aerosols as heterogeneous ice nuclei, *Geophys. Res. Lett.*, 40, 4121–4126,
955 <https://doi.org/10.1002/grl.50794>, 2013.

956 Zaveri, R. A., Easter, R. C., Fast, J. D., and Peters, L. K.: Model for Simulating Aerosol
957 Interactions and Chemistry (MOSAIC), *J. Geophys. Res.-Atmo.*, 113,
958 <https://doi.org/https://doi.org/10.1029/2007jd008782>, 2008.

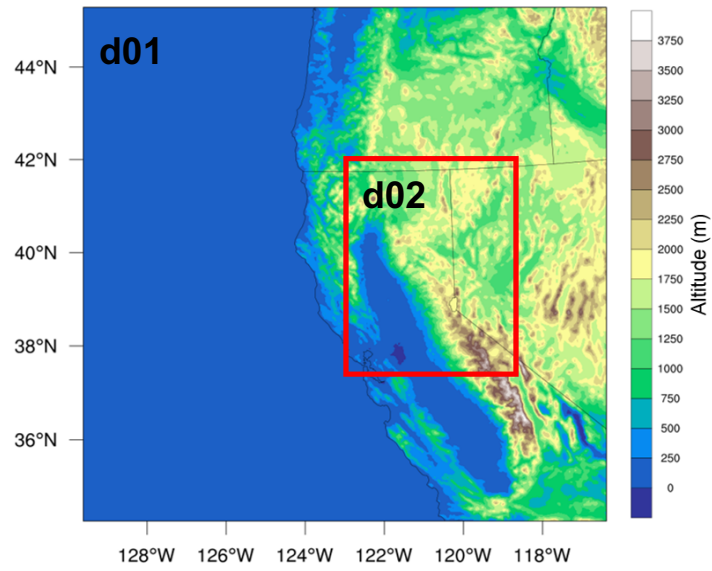
959 Zhang, Y., Fan, J., Li, Z., and Rosenfeld, D.: Impacts of Cloud Microphysics Parameterizations
960 on Simulated Aerosol–Cloud-Interactions for Deep Convective Clouds over Houston,
961 *Atmos. Chem. Phys.*, 1–46, <https://doi.org/10.5194/acp-2020-372>, 2020.

962 Zhao, B., Wang, Y., Gu, Y., Liou, K.-N., Jiang, J. H., Fan, J., Liu, X., Huang, L., and Yung, Y.
963 L.: Ice nucleation by aerosols from anthropogenic pollution, *Nature Geosciences*, 12,
964 <https://doi.org/10.1038/s41561-019-0389-4>, 2019.

965 Zhao, C., Chen, S., Leung, L. R., Qian, Y., Kok, J. F., Zaveri, R. A., and Huang, J.: Uncertainty
966 in modeling dust mass balance and radiative forcing from size parameterization, *Atmos.*
967 *Chem. Phys.*, 13, 10733–10753, <https://doi.org/10.5194/acp-13-10733-2013>, 2013

968
969

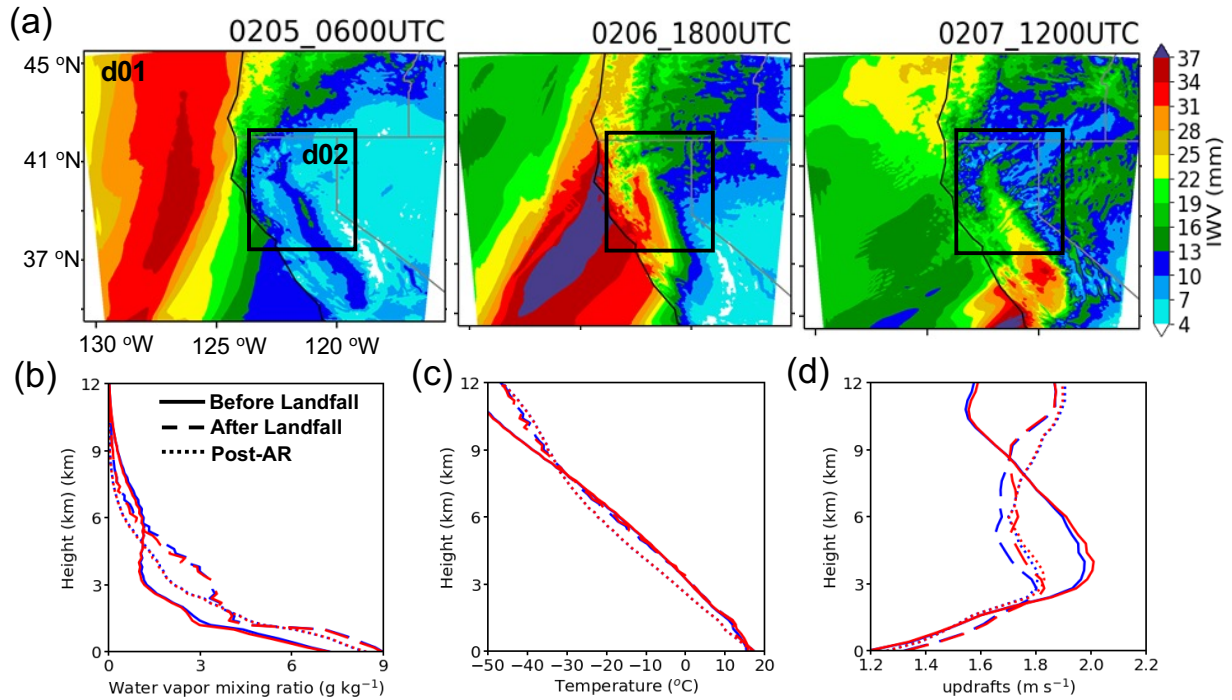
970 **Figures**



971

972 **Figure 1.** Two nested simulation domains: d01 and d02 centering over California. The color
973 shading denotes the terrain elevation.

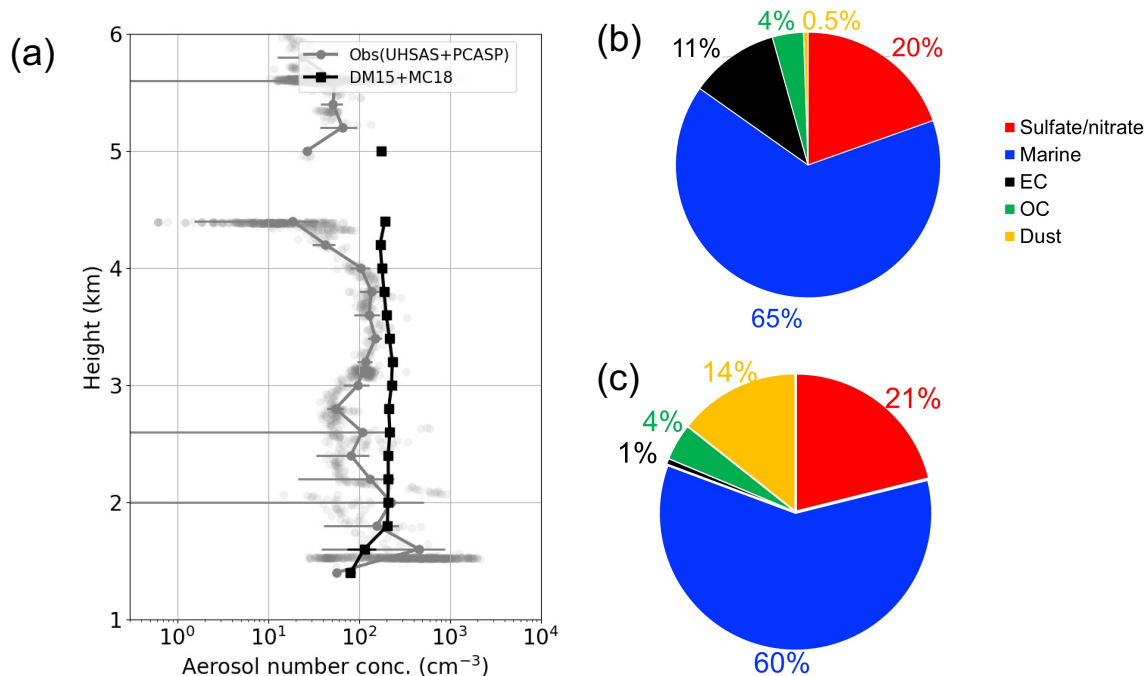
974



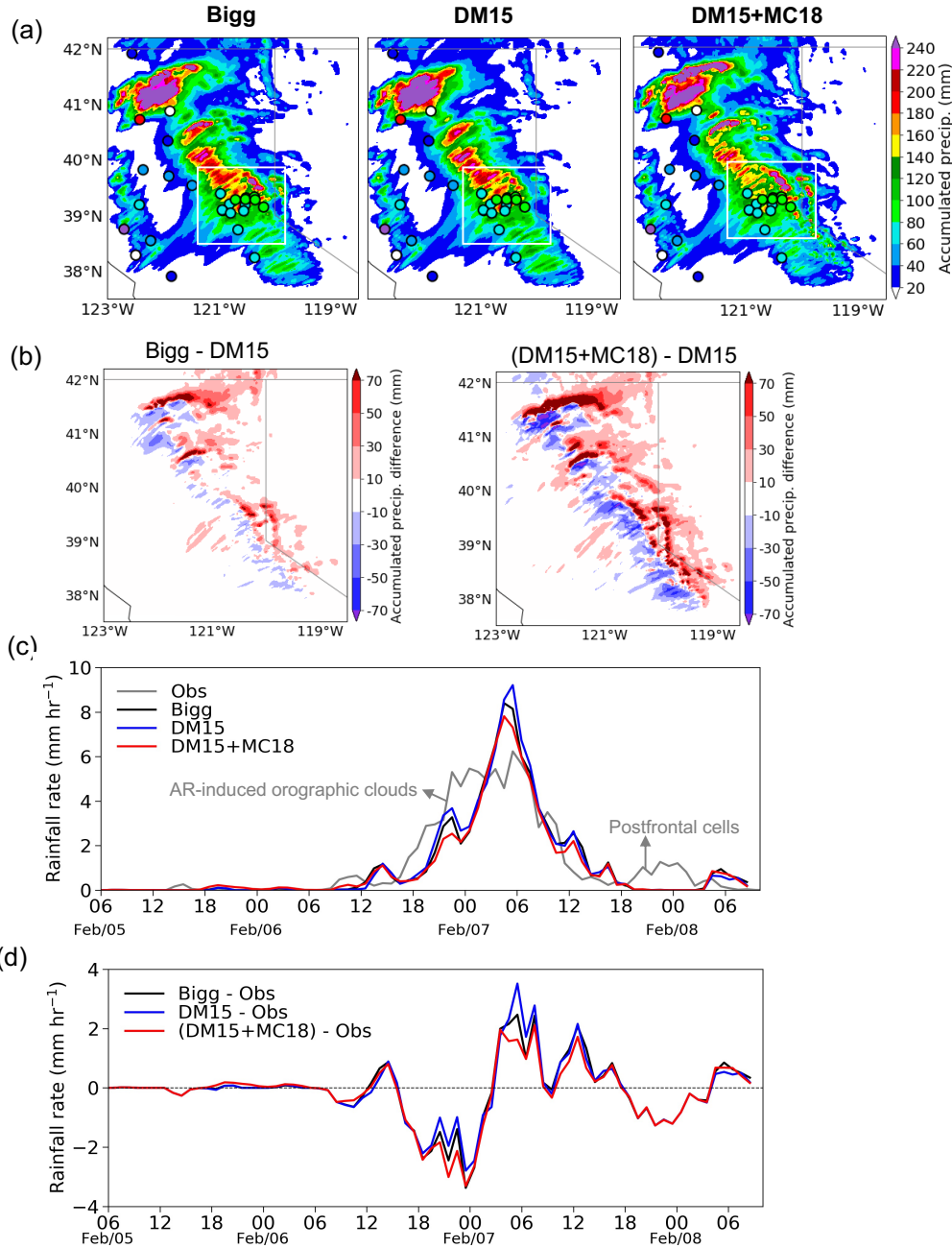
975

976 **Figure 2.** (a) Evolution of integrated water vapor (IWV) at 06:00 UTC 5 February (before AR
 977 landfall), 18:00 UTC 6 February (after AR landfall), and 12:00 UTC 7 February (post-AR). The
 978 black box (i.e., d02) in (a) is the domain of this study with the 5 lateral boundary grids excluded
 979 for analysis at each side. (b-d) show the mean vertical profiles of (b) water vapor mixing ratio,
 980 (c) temperature, and (d) updraft velocity at the three AR stages, i.e., before (solid lines) and after
 981 (dashed lines) AR landfall and post-AR stages (dotted lines), for the simulations of DM15 (blue)
 982 and DM15+MC18 (red). The water vapor mixing ratio and temperature are averaged for cloud-
 983 free grids, and updraft velocity is averaged over the grids with a vertical velocity greater than 1
 984 m s⁻¹.

985

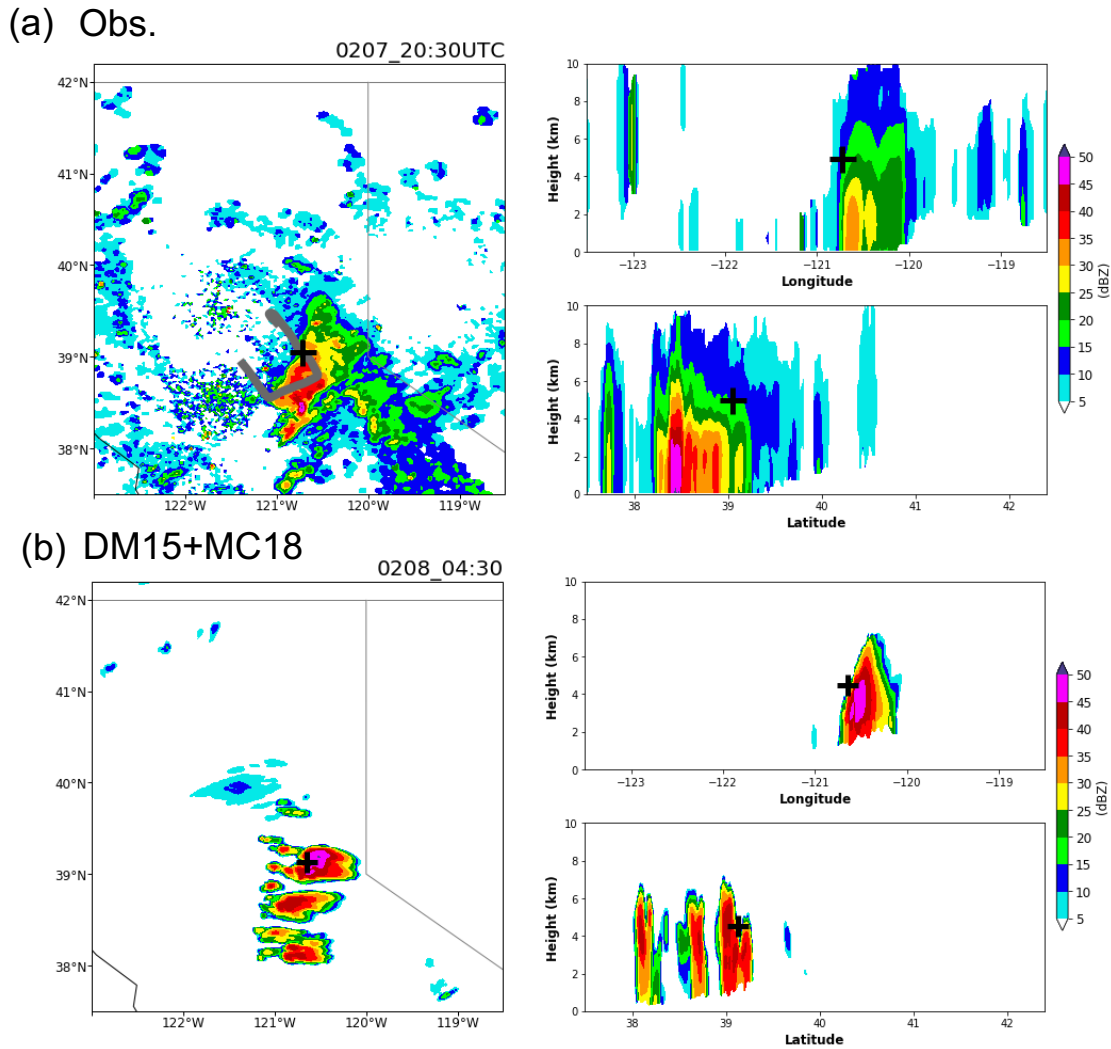


986
 987 **Figure 3.** (a) Vertical distributions of aerosol number concentrations from aircraft observations
 988 (Obs, grey) and DM15+MC18 (black) for particles with a dry diameter over a range of 0.067~3
 989 μm , (b) mean fractional number contributions of aerosol classifications based on measurements
 990 of single-particle mass spectra of aerosols and cloud particle residuals reported in Levin et al.
 991 (2019), and (c) mean fractional mass contributions of aerosols in DM15+MC18 (number
 992 concentration for each aerosol component is not predicted by WRF-Chem). The aerosol number
 993 concentration from aircraft observations in (a) consists of both measurements from UHSAS and
 994 PCASP. The modeled data in (a) and (c) are sampled along the aircraft route on 7 February 2015.

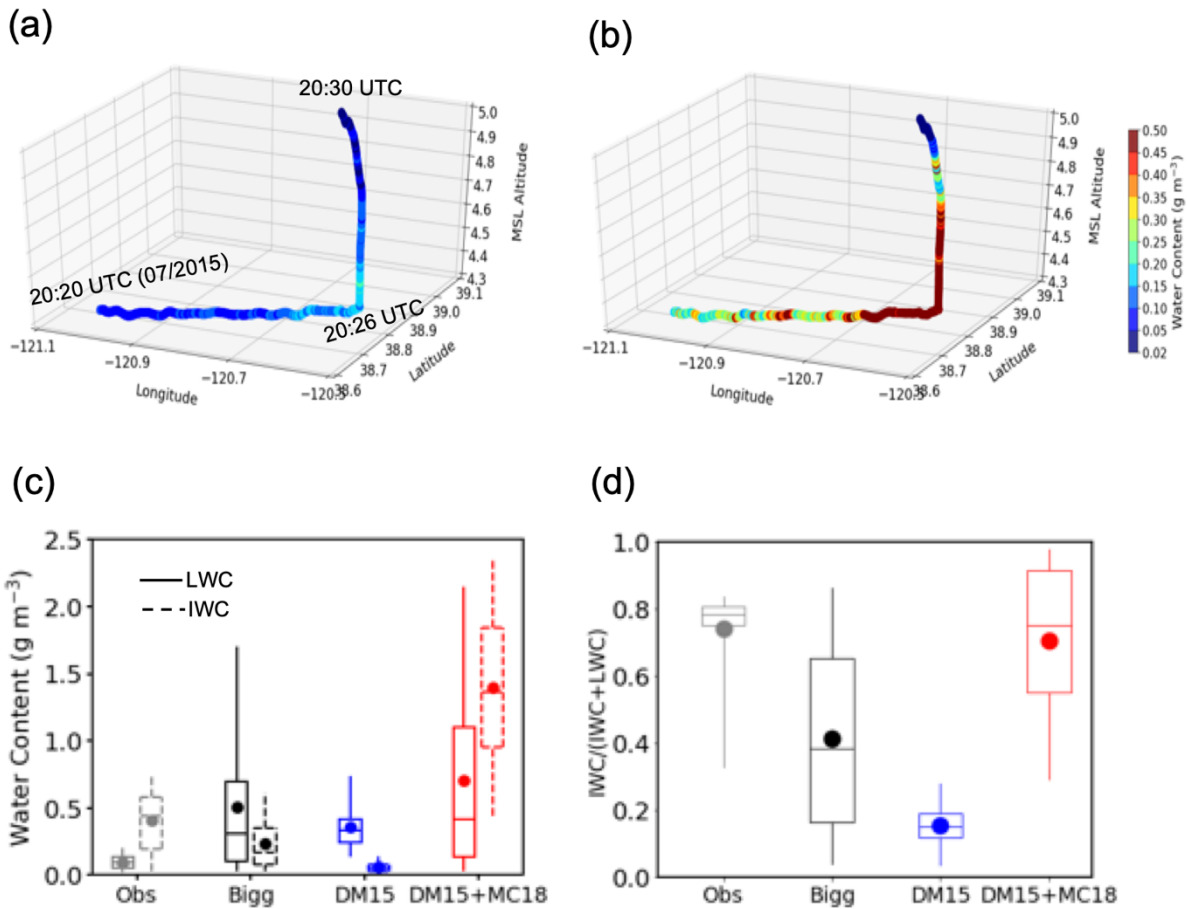


995

996 **Figure 4.** (a) Spatial distributions of accumulated precipitation during the AR event (5 Feb.
 997 06:00 – 8 Feb. 09:00 UTC) from Bigg, DM15, and DM15+MC18. The color shading is for
 998 simulations and the circles denote the rain gauge measurements provided by NOAA Physical
 999 Sciences Laboratory. (b) as (a) but for differences between Bigg and DM15 (left) and between
 1000 DM15+MC18 and DM15 (right). (c) Time series of precipitation rates during the entire AR
 1001 event for rain gauge observations (grey line), Bigg (black line), DM15 (blue line), and
 1002 DM15+MC18 (red line). (d) Differences between the simulations and observations based on the
 1003 data of (b). The precipitation rates in (b) are averaged over all the rain gauge sites shown in (a).
 1004 The white boxes in (a) mark the region where the precipitation simulation is improved by adding
 1005 marine INPs.

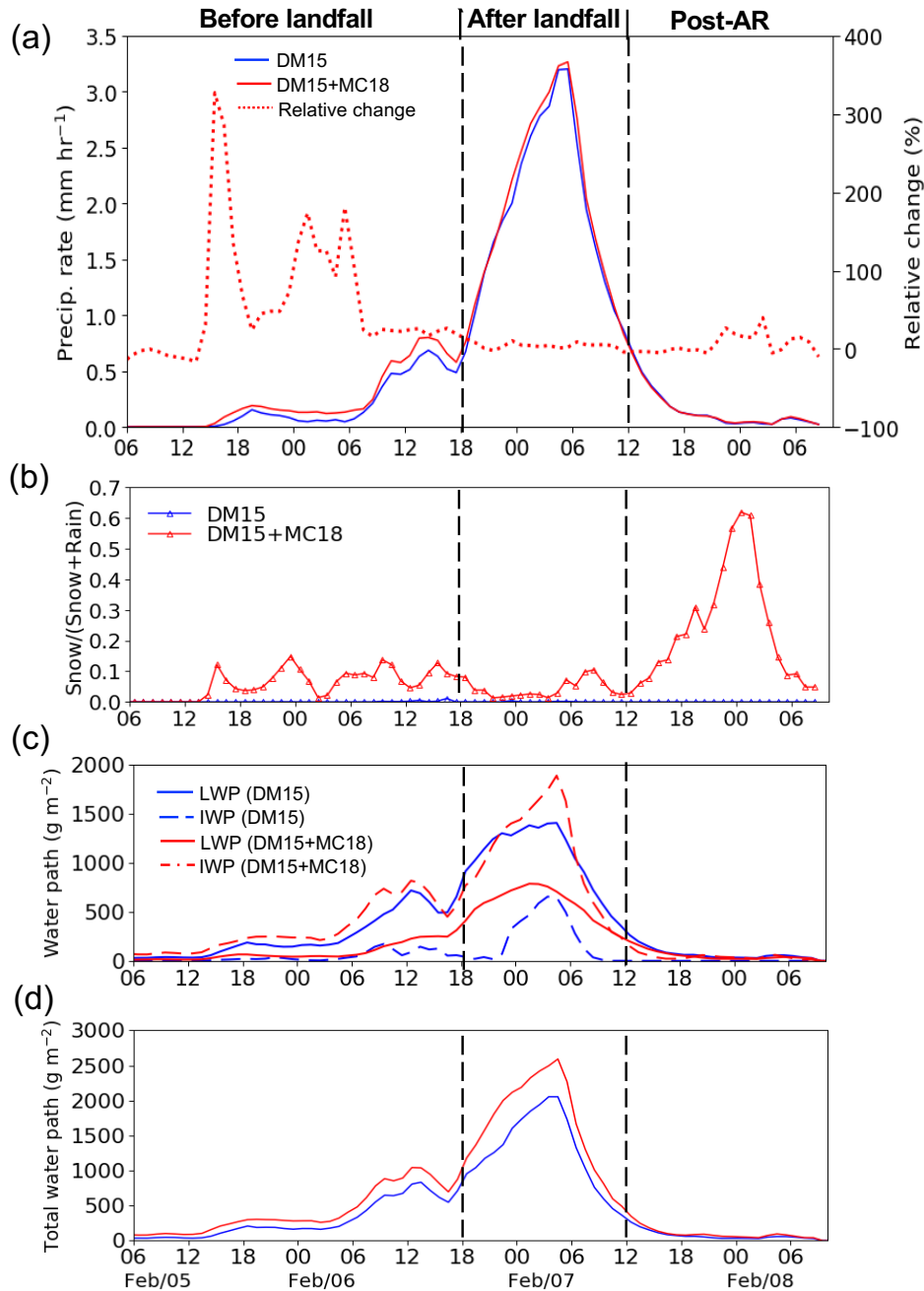


1006
 1007 **Figure 5.** (a) Composite reflectivity of NEXRAD for the postfrontal clouds that the G-1 aircraft
 1008 sampled, (b) composite reflectivity from the simulation of DM15+MC18 for the postfrontal
 1009 clouds. The observation and simulation are compared at the peak reflectivity time which is 20:30
 1010 UTC 7 February for the observed clouds and 04:30 UTC 8 February for the simulated clouds.
 1011 The black crosses in the left two panels denote the positions where the longitude-height and
 1012 latitude-height cross-sections in the right panels are plotted. The grey line in the left panel of (a)
 1013 shows the flight track of the G-1 aircraft.



1014
1015

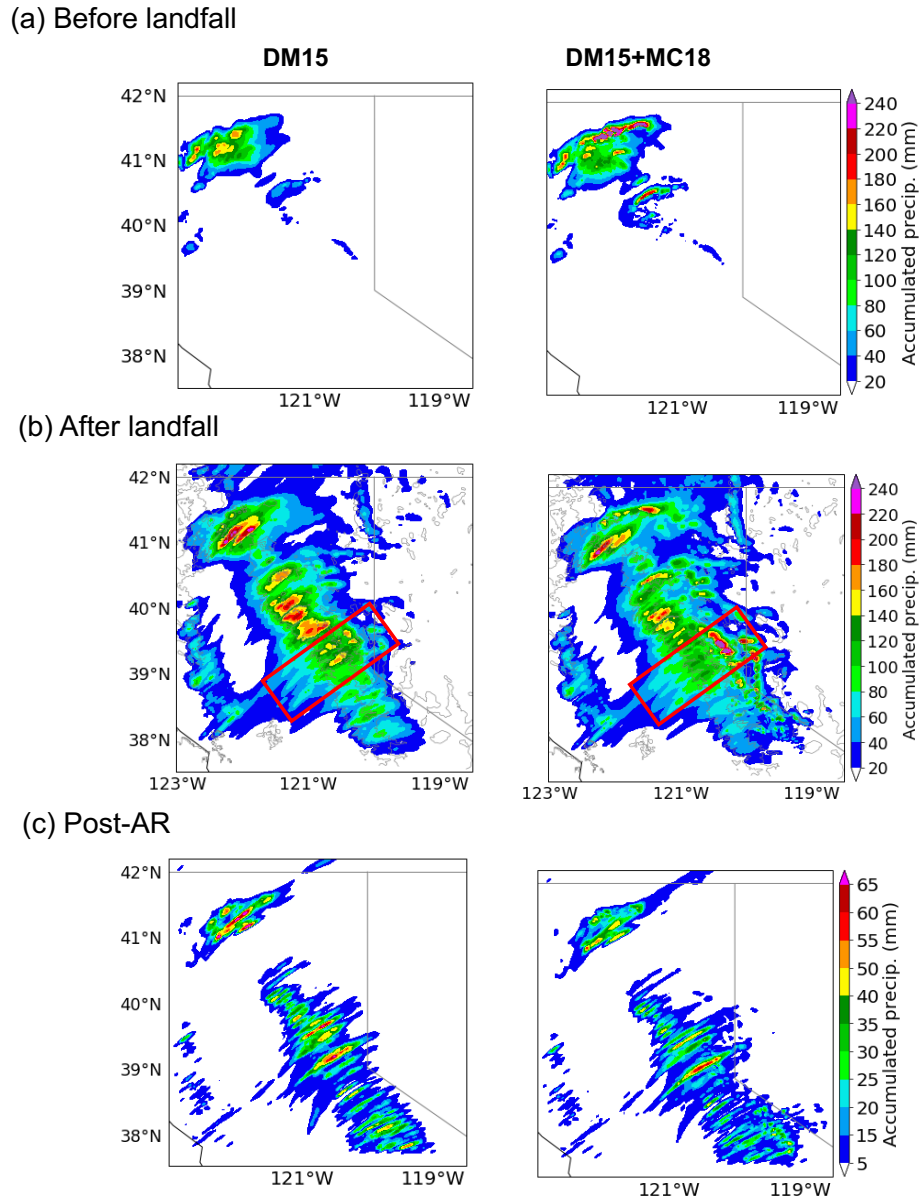
1016 **Figure 6.** Comparisons of the simulations with aircraft observations. The observed (a) LWC and
 1017 (b) IWC along the flight track during 20:20 – 20:30 on 7 February when the aircraft flew through
 1018 the mixed-phase regime of the postfrontal clouds. (c) LWC (solid) and IWC (dashed) and (d) the
 1019 glaciation ratios of $\text{IWC}/(\text{IWC}+\text{LWC})$ from the aircraft measurements (Obs, grey) and
 1020 simulations of Bigg (black), DM15 (blue), and DM15+MC18 (red). The boxes show the 25th,
 1021 median (horizontal lines in the box), and 75th percentiles of the data. The upper and lower
 1022 whiskers show the 95th and 5th percentiles, respectively. The mean values are denoted by circles.
 1023



1024

1025 **Figure 7.** Time series of (a) precipitation rate (solid lines, left y-axis), (b) ratio of snow
 1026 precipitation (i.e., snow/(snow+rain) in mass mixing ratio) at the lowest model level, (c) LWP
 1027 (solid) and IWP (dashed) for DM15 (blue) and DM15+MC18 (red), and (d) total condensate
 1028 water path (TWP). The relative changes in precipitation rate from DM15 to DM15+MC18 are
 1029 shown in the red dotted line in (a) with values shown on the right y-axis. The vertical dashed
 1030 lines divide the three AR stages.

1031



1032

1033

1034

1035

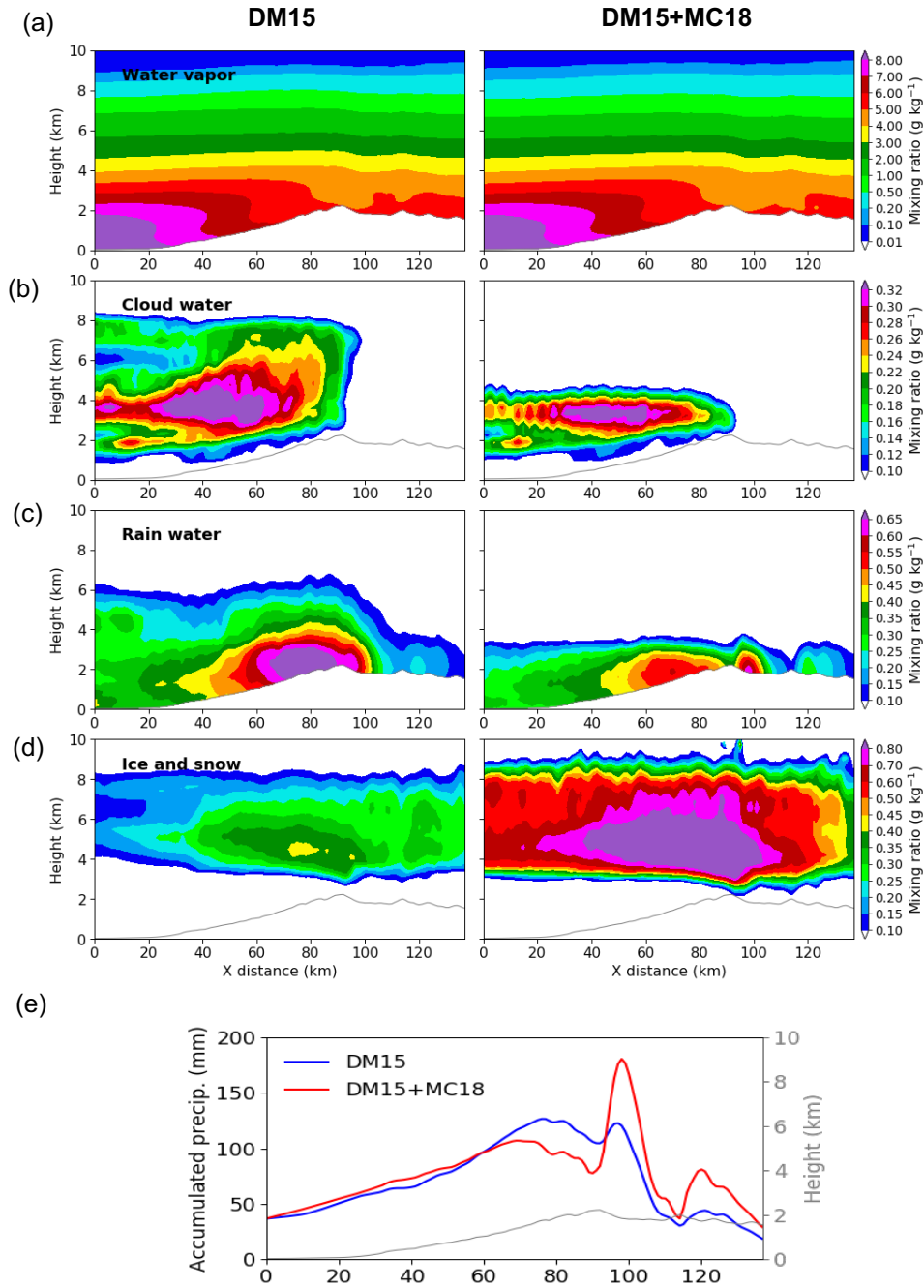
1036

1037

1038

1039

Figure 8. Spatial distribution of accumulated precipitation during the stages of (a) before AR landfall, (b) after AR landfall, and (c) post-AR in DM15 (left) and DM15+MC18 (right). The parallelograms marked in (b) denotes the area for the east-west cross-section analysis shown in Figure 9.



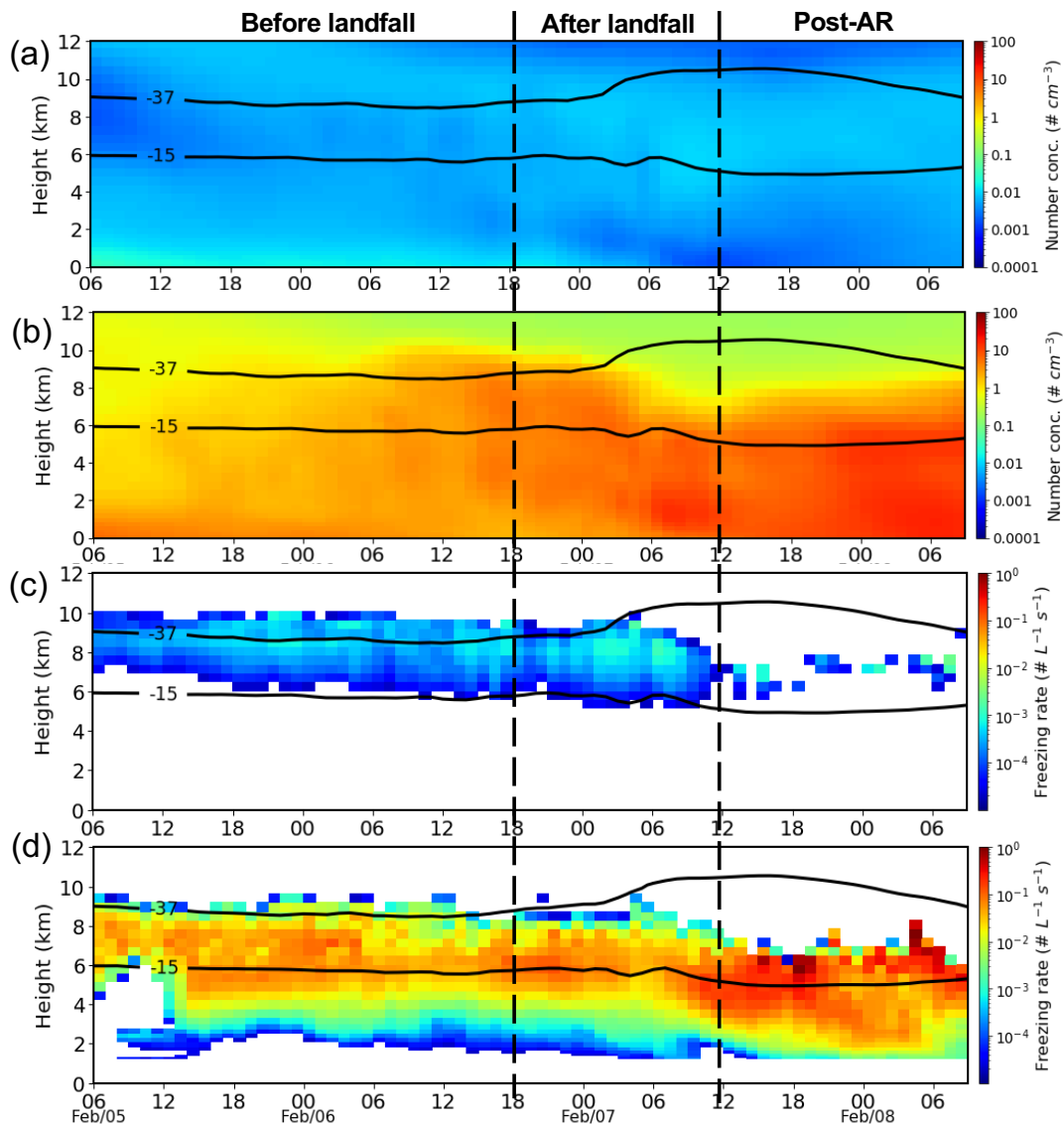
1040

1041

1042 **Figure 9.** Mean mixing ratios of (a) water vapor, (b) cloud water, (c) rainwater, (d) ice + snow,

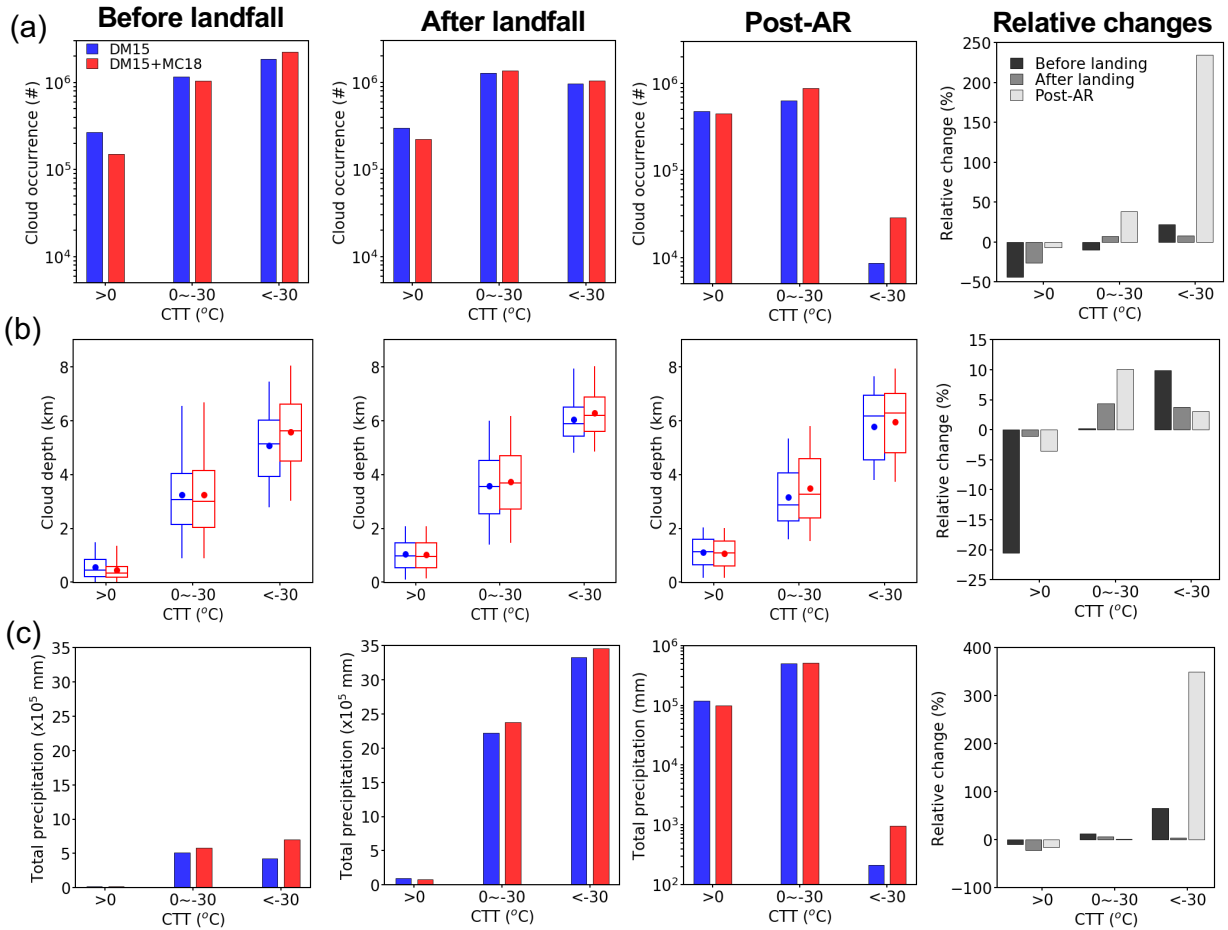
1043 and (e) surface precipitation at the stage after AR landfall in DM15 and DM15+MC18. The

1044 vertical cross-sections are averaged over the red boxes marked in Fig. 8b and the entire stage.



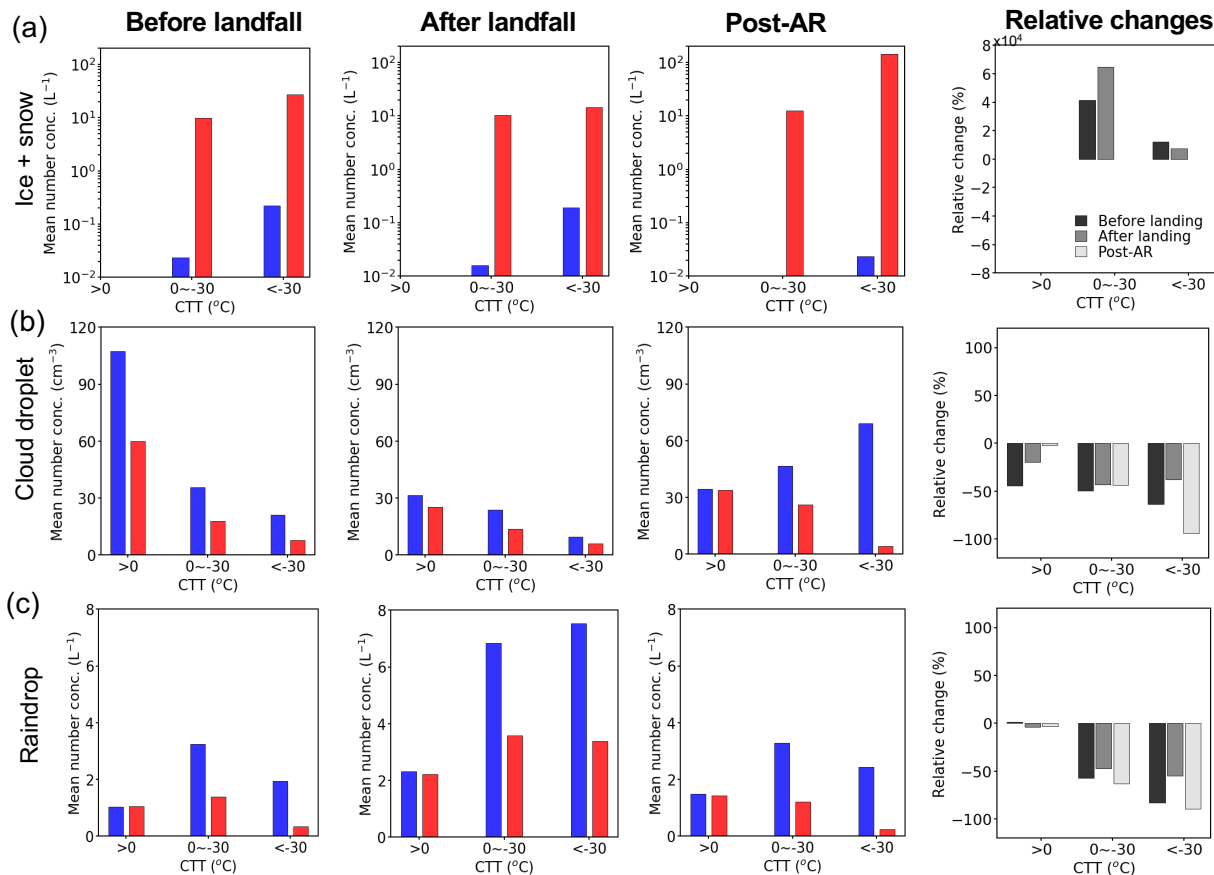
1046

1047 **Figure 10.** Time-height cross-sections of (a) dust particle ($>0.5 \mu\text{m}$) number concentration, (b)
 1048 marine aerosol number concentration, (c) the freezing rate in DM15, and (d) the freezing rate in
 1049 DM15+MC18. The number concentrations in (a) and (b) are derived from their corresponding
 1050 mass mixing ratios under the clear-sky condition only. The freezing rates in (c) and (d) are the
 1051 ice nucleation rates via immersion freezing at $T > -37 \text{ }^\circ\text{C}$ and the drop homogenous freezing
 1052 rates at $T < -37 \text{ }^\circ\text{C}$, and the values are for cloudy-points only. The black contour lines in each
 1053 panel mark the temperature levels of -15 and $-37 \text{ }^\circ\text{C}$, representing the efficient immersion
 1054 freezing temperature in DM15+MC18 and the homogeneous freezing temperature in the model,
 1055 respectively.

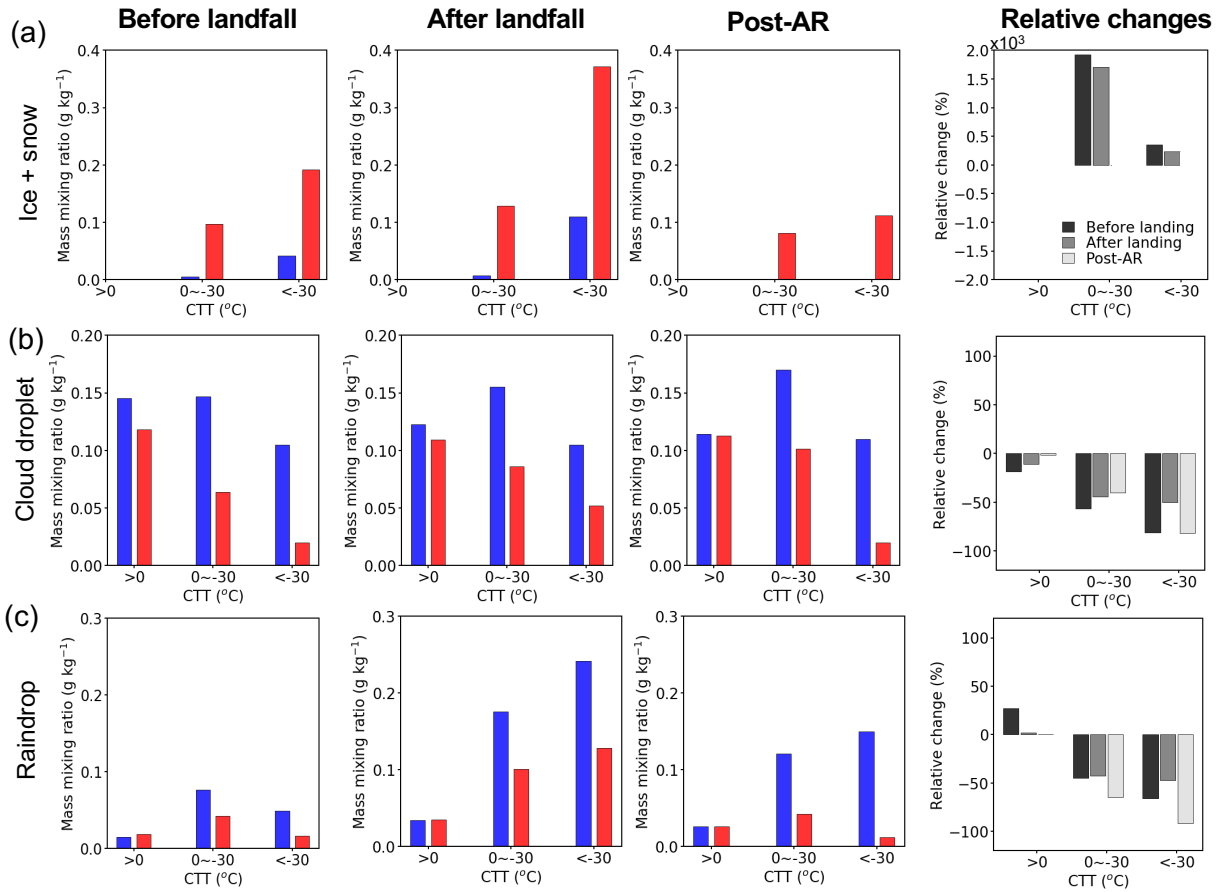


1057

1058 **Figure 11.** (a) Cloud occurrences, (b) cloud depth, and (c) total precipitation for three cloud
 1059 regimes in DM15 (blue) and DM15+MC18 (red) at three AR stages from left to right: before AR
 1060 landfall, after AR landfall, post-AR. The last column shows the relative changes caused by the
 1061 marine INP effect, which are calculated as $[(DM15+MC18) - DM15]/DM15 * 100\%$. Note that
 1062 the total precipitation at the post-AR stage uses a log scale for the y-axis. The box-whisker plots
 1063 follow the description in Figure 5c.



1064
 1065 **Figure 12.** Hydrometeor number concentrations and their relative changes in three cloud regimes
 1066 in DM15 (blue) and DM15+MC18 (red) at the three AR stages for (a) ice particles (sum of ice
 1067 and snow), (b) cloud droplets, and (c) raindrops. The last column shows the relative changes
 1068 caused by the marine INP effect, which are calculated as $[(DM15+MC18) -$
 1069 $DM15]/DM15 \cdot 100\%$. Since ice particles are very limited at the post-AR stage in DM15, the
 1070 percentage changes of ice particles from DM15 to DM15+MC18 are huge numbers that are
 1071 omitted from the plots.



1072

1073 **Figure 13.** Same as Figure 12, except for the mass mixing ratios of (a) ice particles (sum of ice
 1074 and snow), (b) cloud droplets, and (c) raindrops.

1075

1076

1077

1078

1079

1080

1081

1082

1083

1084

1085 **Table 1.** The changes in total precipitation, total condensate water path (TWP), liquid water path
 1086 (LWP), and ice water path (IWP), and cloud fractions (CF), net cloud radiative forcing (CRF) at
 1087 TOA from DM15 to DM15+MC18 (i.e., the marine INP effect), as well as the glaciation ratio,
 1088 i.e., $IWC/(LWC+IWC)$, and the ratios of snow precipitation, i.e., $snow/(rain+snow)$ in mass
 1089 mixing ratio at the lowest model level from DM15 to DM15+MC18, at the three AR stages. The
 1090 percentage changes are calculated following $((DM15+MC18) - DM15)/DM15 * 100$.

1091

AR stages		Before landfall	After landfall	Post-AR
Total precipitation		36%	4%	-1%
TWP		45%	29%	35%
LWP		-66%	-46%	-26%
IWP		8 times	5 times	440 times
CF		5%	4%	20%
Net CRF at TOA		15%	13%	10%
IWC/(LWC+IWC)	DM15	0.14	0.16	0.001
	DM15+MC18	0.74	0.59	0.36
Snow/(Rain+Snow)	DM15	0.002	0.001	<0.001
	DM15+MC18	0.085	0.042	0.131

1092

1093

1094 **Table 2.** The domain-mean mass rates of deposition and riming in the mixed-phase and deep
 1095 cloud regimes in DM15 and DM15+MC18 at the three AR stages.

AR stages		Before landfall		After landfall		Post-AR	
		Mixed-phase clouds	Deep clouds	Mixed-phase clouds	Deep clouds	Mixed-phase clouds	Deep clouds
Deposition (mg kg ⁻¹ h ⁻¹)	DM15	44	171	81	388	7	8
	DM15+MC18	846	780	1128	1397	781	1013
Riming (mg kg ⁻¹ h ⁻¹)	DM15	27	89	57	297	25	34
	DM15+MC18	377	228	575	858	505	361

1096

1097